J. Fluid Mech. (2014), *vol.* 758, *pp.* 754–785. © Cambridge University Press 2014
doi:10.1017/jfm.2014.559

Vortex stretching and compression near the turbulent/non-turbulent interface in a planar jet

Tomoaki Watanabe[1,†], Yasuhiko Sakai[1], Kouji Nagata[1], Yasumasa Ito[1] and Toshiyuki Hayase[2]

[1]Department of Mechanical Science and Engineering, Nagoya University, Nagoya 464-8603, Japan

[2]Institute of Fluid Science, Tohoku University, Sendai 980-8577, Japan

(Received 23 March 2014; revised 11 August 2014; accepted 21 September 2014;
first published online 13 October 2014)

Vortex stretching and compression, which cause enstrophy production by inviscid processes, are investigated near the turbulent/non-turbulent (T/NT) interface in a planar jet by using a direct numerical simulation (DNS). The enstrophy production is investigated by analysing the relationship among a vorticity vector, strain-rate eigenvectors and strain-rate eigenvalues. The statistics are calculated individually for three different interface orientations. The vorticity near the T/NT interface is oriented in the tangential direction to the interface. The enstrophy production is affected by the interface orientation because the intensity of vortex stretching depends on the interface orientation, and the alignment between the vorticity vector and the strain-rate eigenvectors is confined by the interface. The enstrophy production near the T/NT interface is analysed by considering the motion of turbulent fluid relative to that of the interface. The results show that the alignment between the interface and the strain-rate eigenvectors changes depending on the velocity field near the T/NT interface. When the turbulent fluid moves toward the T/NT interface, the enstrophy is generated by vortex stretching without being greatly affected by vortex compression. In contrast, when the turbulent fluid relatively moves away from the T/NT interface, large enstrophy reduction frequently occurs by vortex compression. Thus, it is shown that the velocity field near the T/NT interface affects the enstrophy production near the interface through the alignment between the vorticity and the strain-rate eigenvectors.

Key words: jets, turbulent flows, vortex dynamics

1. Introduction

Interfaces dividing turbulent and non-turbulent regions appear in free shear flows, such as wakes, jets and mixing layers. These interfaces are called turbulent/non-turbulent (T/NT) interfaces (da Silva *et al.* 2014). Because free shear flows can be observed in many environmental and industrial flows, predicting and controlling their development is important. Free shear flows develop by converting non-turbulent fluid near the T/NT interface into turbulent fluid. This conversion causes entrainment of the non-turbulent fluid. Therefore, the development of free shear flows strongly depends on the characteristics of the T/NT interface.

† Email address for correspondence: watanabe.tomoaki@c.nagoya-u.jp

https://doi.org/10.1017/jfm.2014.559 Published online by Cambridge University Press

The scales which dominate the entrainment process have been discussed over the years, and the large scales have been considered to dominate it (e.g. Townsend 1976; Mungal & Hollingsworth 1989). In contrast, Corrsin & Kistler (1955) emphasized the importance of the small scales in the entrainment. The role of the T/NT interface in the entrainment has been investigated recently by using numerical simulations and experiments. Westerweel and coworkers have revealed that small-scale eddies near the T/NT interface make a large contribution to the entrainment process by experimentally investigating a round jet (Westerweel *et al.* 2002, 2005, 2009). However, not only the small-scale eddies near the T/NT interface but also the large-scale motions of non-turbulent fluid are responsible for the total entrainment process (Philip & Marusic 2012). Therefore, for investigating the dominant scales of the entrainment process, further investigations, such as multiscale analysis (de Silva *et al.* 2013; Philip *et al.* 2014), are required. Chauhan *et al.* (2014) investigated the T/NT interface in the boundary layer at high Reynolds numbers, and showed that the entrainment in the boundary layer is characterized by two different length scales.

Because the turbulent region is characterized by high enstrophy, the entrainment process has been investigated by analysing the enstrophy transport near the T/NT interface. Holzner *et al.* (2008) and Holzner & Lüthi (2011) experimentally investigated a turbulent front generated by an oscillating grid, where mean shear does not exist. They derived an expression for the velocity of the T/NT interface propagation, which is called local entrainment velocity, by analysing the enstrophy transport equation. Holzner & Lüthi (2011) showed that the propagation of the T/NT interface is dominated by the viscous diffusion of the enstrophy. However, Wolf *et al.* (2012) experimentally investigated the local entrainment velocity in a turbulent jet, and showed that vortex stretching, which is an inviscid process, also has the potential to cause the local entrainment. They also analysed the alignment between the vorticity and eigenvectors of the rate-of-strain tensor at the T/NT interface, and showed that the alignment can be related to the entrainment process by vortex stretching.

The T/NT interface consists of two layers: a turbulent sublayer (da Silva *et al.* 2014) and a viscous superlayer (Corrsin & Kistler 1955). The increase in the enstrophy is dominated by the viscous effects in the viscous superlayer, but is caused by the inviscid and viscous processes in the turbulent sublayer (Taveira & da Silva 2014). Therefore, the relative importance of the inviscid and viscous effects depends on the threshold value used for defining the interface (van Reeuwijk & Holzner 2014). Taveira *et al.* (2013) used direct numerical simulations (DNS) of a temporally developing jet (da Silva & Pereira 2004) to investigate the Lagrangian statistics near the T/NT interface. Their analysis of the enstrophy transport equation revealed that the enstrophy growth in the non-turbulent region near the T/NT interface is caused by viscous diffusion, whereas the enstrophy production by the inviscid process dominates its generation inside the turbulent region. As shown in the previous investigations on enstrophy transport, the increase in the enstrophy near the T/NT interface is not only caused by viscous diffusion, but also by the inviscid process. In this study, the inviscid contribution to the enstrophy generation near the T/NT interface is investigated in detail.

The enstrophy $\omega^2/2 \equiv \omega_i\omega_i/2$ evolves according to the following transport equation:

$$\frac{\mathrm{D}\omega^2/2}{\mathrm{D}t} = \omega_i S_{ij}\omega_j + \nu\nabla^2(\omega^2/2) - \nu\nabla\omega_i \cdot \nabla\omega_i. \tag{1.1}$$

Here, $\omega_i = \epsilon_{ijk}\partial U_k/\partial x_j$ is the i-direction component of the vorticity vector (where ϵ_{ijk} is the Levi-Civita symbol), $S_{ij} = (\partial U_i/\partial x_j + \partial U_j/\partial x_i)/2$ is the component of the

https://doi.org/10.1017/jfm.2014.559 Published online by Cambridge University Press

rate-of-strain tensor, U_i is the i-direction velocity and ν is the kinematic viscosity. The first term on the right-hand side of (1.1) is the production term, which is caused by the inviscid process, the second term is the viscous diffusion term and the third term is the viscous dissipation term. The enstrophy production term consists of ω_i and S_{ij} and is the scalar product of the vorticity vector ω_i with the vortex stretching vector $S_{ij}\omega_j$. Therefore, the interaction between the vorticity and strain fields determines the enstrophy production. The rate-of-strain tensor has three real eigenvalues s_i, where s_i is arranged in descending order (i.e. $s_1 \geqslant s_2 \geqslant s_3$). For an incompressible flow, $s_1 + s_2 + s_3 = 0$ because of the continuity equation. Therefore, the eigenvalue s_1 is always positive and corresponds to the extensive strain rate, whereas s_3, which is always negative, corresponds to the compressive strain rate. The intermediate strain-rate eigenvalue s_2 can be positive or negative, and s_1 and s_3 are bounds for s_2. The eigenvector corresponding to s_i is denoted by $\boldsymbol{e}_i$. The eigenvectors of s_i are orthogonal to each other. By using the eigenvalues and eigenvectors of S_{ij}, the enstrophy production $\omega_i S_{ij}\omega_j$ is represented by

$$\omega_i S_{ij}\omega_j = \omega^2 s_i(\hat{\boldsymbol{\omega}} \cdot \boldsymbol{e}_i)^2. \tag{1.2}$$

Here, $\hat{\boldsymbol{\omega}} \equiv \boldsymbol{\omega}/|\boldsymbol{\omega}|$ is the unit vorticity vector. Equation (1.2) shows that s_i determines the intensity of vortex stretching or compression in the direction of $\boldsymbol{e}_i$. The inner product $\hat{\boldsymbol{\omega}} \cdot \boldsymbol{e}_i$ is the cosine of the alignment angle between the vorticity vector and the eigenvector for s_i. Vortex stretching or compression by s_i effectively acts on vorticity when its eigenvector $\boldsymbol{e}_i$ aligns with the vorticity vector. Therefore, the alignment between the vorticity vector and the strain-rate eigenvectors is important in enstrophy production. Previous studies showed that the vorticity vector preferentially aligns with the intermediate strain-rate eigenvector $\boldsymbol{e}_2$ and is perpendicular to the compressive strain-rate eigenvector $\boldsymbol{e}_3$ (Ashurst *et al.* 1987; Jiménez 1992; Tanahashi, Iwase & Miyauchi 2001; Buxton & Ganapathisubramani 2010). Although the extensive strain-rate eigenvector $\boldsymbol{e}_1$ arbitrarily aligns with the vorticity vector, the enstrophy production term tends to be positive when $\boldsymbol{e}_1$ aligns with the vorticity vector (Buxton & Ganapathisubramani 2010).

The T/NT interface envelops the high-enstrophy region and appears along the vortical structures in the turbulent region (da Silva, Dos Reis & Pereira 2011). da Silva & Taveira (2010) showed that the thickness of the T/NT interface is almost equal to the radius of large vorticity structures near the interface. Because the vortical structures do not exist in the non-turbulent region, the vorticity in the turbulent region cannot penetrate the T/NT interface, and the spatial distribution of the vorticity is confined by the presence of the interface. Therefore, the vorticity near the T/NT interface tends to align with the direction tangential to the interface (da Silva & dos Reis 2011). This confinement of the vorticity distribution near the interface is expected to affect the alignment between the vorticity and strain-rate eigenvectors. In this study, we analyse the relationships among the T/NT interface orientation, the vorticity vector and the strain-rate eigenvectors and eigenvalues near the T/NT interface in a planar jet to investigate enstrophy generation and reduction by vortex stretching and compression. Unlike Wolf *et al.* (2012), we investigate the alignment between the vorticity and strain-rate eigenvectors in the turbulent region near the interface, where the enstrophy growth is caused on average by the inviscid process (Taveira *et al.* 2013). DNS results for the planar jet (Watanabe *et al.* 2013*b*, 2014*a*) are used in this study. We also focus on large-scale motion in the turbulent region, which characterizes the interface geometry and velocity field near the T/NT interface,

https://doi.org/10.1017/jfm.2014.559 Published online by Cambridge University Press

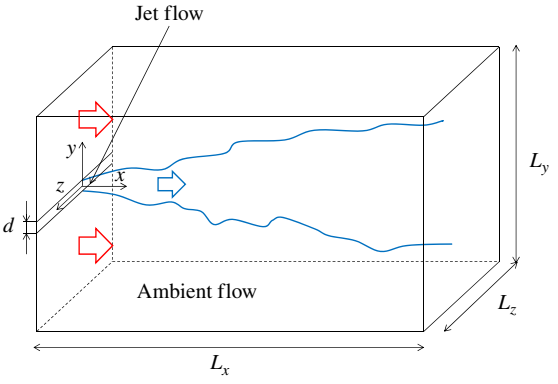


FIGURE 1. (Colour online) Computational domain of a planar jet.

and investigate its role in vortex stretching and compression near the interface. Conditional sampling methods have been used for investigating turbulent fronts and trailing edges in experiments using hot-wire anemometry. In this study, the invariants of velocity gradient and strain-rate tensors and the enstrophy production, which are not easy to measure in experiments using hot-wire anemometry, are analysed for different interface orientations. Section 2 describes the DNS of the planar jet and the procedure for the T/NT interface detection. The numerical results are presented in § 3. Finally, the conclusions are summarized in § 4.

2. Direct numerical simulation of a planar jet

2.1. *Numerical method and computational parameters*

The spatially developing planar jet described in figure 1 is investigated using DNS. The origin of the coordinate system is located at the centre of the jet inlet. The streamwise, lateral and spanwise directions are represented by x, y and z, respectively. The size of the computational domain is $L_x \times L_y \times L_z = 9.0\pi d \times 7.3\pi d \times 1.2\pi d$, where d is the width of the jet inlet. The governing equations are the continuity equation and Navier–Stokes equations for an incompressible flow, which are written as follows:

$$\frac{\partial U_j}{\partial x_j} = 0, \tag{2.1}$$

$$\frac{\partial U_i}{\partial t} + \frac{\partial U_j U_i}{\partial x_j} = -\frac{\partial p}{\partial x_i} + \nu \frac{\partial^2 U_i}{\partial x_j \partial x_j}, \tag{2.2}$$

where U_i is the instantaneous velocity, p is the instantaneous pressure divided by the density and ν is the kinematic viscosity.

The governing equations are solved using a finite difference method. The fully conservative fourth-order central difference scheme proposed by Morinishi *et al.* (1998) is used for spatial discretization in the x and z directions, and the fully conservative second-order central difference scheme (Morinishi *et al.* 1998) is used in the y direction because the second-order scheme does not require special treatment for non-equidistant grids. The advection term in (2.2) is discretized using a skew-symmetric form for suppressing aliasing errors. Equations (2.1) and (2.2) are solved using the fractional step method. The Poisson equation is solved by the fast

https://doi.org/10.1017/jfm.2014.559 Published online by Cambridge University Press

n	0	1	2	3	4	5
A_n	1.303×10^{0}	-9.236×10^{-1}	-8.571×10^{0}	-1.207×10^{2}	3.464×10^{2}	0
$B_{u,n}$	4.673×10^{-2}	5.470×10^{-2}	-1.368×10^{0}	1.043×10^{1}	-1.657×10^{1}	0
$B_{v,n}$	3.505×10^{-2}	-1.558×10^{-2}	5.192×10^{-1}	-1.249×10^{0}	0	0
$B_{w,n}$	3.505×10^{-2}	-3.551×10^{-3}	1.930×10^{-1}	-1.186×10^{0}	7.355×10^{0}	-1.267×10^{1}

TABLE 1. Coefficients in (2.3)–(2.6) used to determine boundary condition at jet inlet.

Fourier transform (in the spanwise direction), the cosine transform (in the streamwise direction) and a tridiagonal matrix algorithm (in the cross-streamwise direction). The Crank–Nicolson method is used for the time integration of the y-direction viscous terms, whereas the third-order Runge–Kutta method is used for the other terms (Spalart, Moser & Rogers 1991).

The Reynolds number based on the width of the jet inlet d and the mean bulk velocity at the jet inlet U_J is $Re = U_J d/\nu = 2200$. There are $N_x \times N_y \times N_z = 2048 \times 600 \times 128$ computational grid points used in the DNS. A uniform grid is used in the x and z directions. In the y direction, a fine grid is used near the jet centreline, and the grid is stretched near the lateral boundaries. A periodic boundary condition is applied in the spanwise (z) direction. At the lateral boundaries, the y directional gradient of velocity is set to 0. The convective boundary condition proposed by Dai, Kobayashi & Taniguchi (1994) is used at the outlet plane. At $x = 0$ in the ambient flow, the cross-streamwise and spanwise velocities are set to zero and the streamwise velocity is $U_A = 0.056U_J$ without any fluctuations. The velocity at the jet inlet ($x = 0$) is generated by superimposing velocity fluctuations on the mean velocity so that the lateral profiles of the streamwise mean velocity (U_{in}) and the root-mean-square (r.m.s.) values of the velocity fluctuations (u_{rms}, v_{rms}, w_{rms}) at the jet inlet satisfy the following equations:

$$\frac{U_{in}(y) - U_A}{U_J} = \sum_{n=0}^{5} A_n \left(\frac{y}{d}\right)^{2n}, \tag{2.3}$$

$$\frac{u_{rms}(y)}{U_J} = \frac{1}{20} \sum_{n=0}^{5} B_{u,n} \left|\frac{y}{d}\right|^{n}, \tag{2.4}$$

$$\frac{v_{rms}(y)}{U_J} = \frac{1}{20} \sum_{n=0}^{5} B_{v,n} \left|\frac{y}{d}\right|^{n}, \tag{2.5}$$

$$\frac{w_{rms}(y)}{U_J} = \frac{1}{20} \sum_{n=0}^{5} B_{w,n} \left|\frac{y}{d}\right|^{n}. \tag{2.6}$$

The coefficients A_n, $B_{u,n}$, $B_{v,n}$ and $B_{w,n}$ are summarized in table 1. The cross-streamwise and spanwise mean velocities are zero at the jet inlet. Equations (2.3) and (2.4) are obtained from the measurement results for $U_{in}(y)$ and $u_{rms}(y)$ in the experimental apparatus used in Watanabe *et al.* (2012, 2013*a*, 2014*b*,*c*). Figure 2(*a*) shows U_{in} given by (2.3) and figure 2(*b*) shows u_{rms}, v_{rms} and w_{rms} given by (2.4), (2.5) and (2.6), respectively. The measurement results for $U_{in}(y)$ and $u_{rms}(y)$ (Watanabe *et al.* 2012, 2013*a*, 2014*b*,*c*) are compared with the above equations in figure 2. The velocity fluctuations which satisfy (2.4)–(2.6) are generated by a diffusion process that converts the random noise into fluctuations which possess the required length

https://doi.org/10.1017/jfm.2014.559 Published online by Cambridge University Press

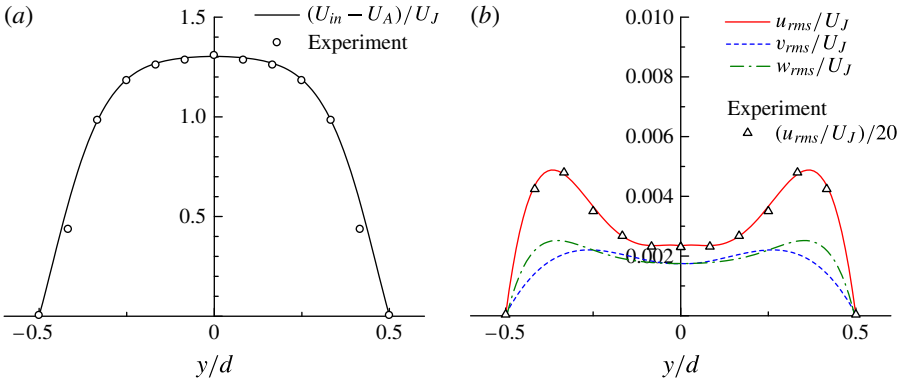


FIGURE 2. (Colour online) (*a*) Mean streamwise velocity and (*b*) r.m.s. values of velocity fluctuations at the jet inlet. Lateral profiles of velocity statistics at the jet inlet are compared with the measurement results (Watanabe *et al.* 2012, 2013*a*, 2014*b*,*c*).

scales (Kempf, Klein & Janicka 2005). According to Stanley, Sarkar & Mellado (2002), the length scale which corresponds to the fundamental mode for the shear layer near the jet inlet is used as the integral length scales of the velocity fluctuations at the jet inlet, which are $0.29d$ in the present DNS. The small velocity fluctuations are used for the boundary conditions at the jet inlet. For the jet development, velocity fluctuations at large scales are important because small-scale fluctuations decay near the jet inlet. The velocity fluctuations generated by the diffusion process contain most of the energy at large scales. Although the total energy represented by the r.m.s. values is small, the velocity fluctuation contains energy at large enough scales to develop the jet flow.

2.2. *Validation of the DNS results*

The time-averaged statistics obtained by the present DNS are compared with previous experimental and numerical studies on planar jets. Figure 3(*a*) shows the mean streamwise velocity $\langle U \rangle$ on the jet centreline, where $\langle\ \rangle$ denotes the time-averaged value. The DNS result agrees well with the experiment by Watanabe *et al.* (2014*b*), which was conducted for the Reynolds number $Re \approx 2200$. Similar to the previous studies on a planar jet (Bradbury 1965; Davies, Keffer & Baines 1975; Stanley *et al.* 2002; Deo, Mi & Nathan 2008), the mean streamwise velocity on the jet centreline is found to evolve according to $(\langle U \rangle - U_A) \propto (x/d)^{-\frac{1}{2}}$. Figures 3(*b*) and 3(*c*) show lateral profiles of the mean streamwise velocity and the jet half-width b_U, respectively. The mean streamwise velocity exhibits a self-similar profile, and b_U increases in proportion to x. Downstream of $x/d = 10$, the mean streamwise velocity and the jet half-width can be represented by

$$\frac{U_J^2}{(\langle U \rangle - U_A)^2} = 0.140(x/d) - 0.0627, \tag{2.7}$$

$$b_U/d = 0.0936(x/d) - 0.0123. \tag{2.8}$$

Thus, the self-similar characteristics in the planar jet can be observed in the mean streamwise velocity profile.

https://doi.org/10.1017/jfm.2014.559 Published online by Cambridge University Press

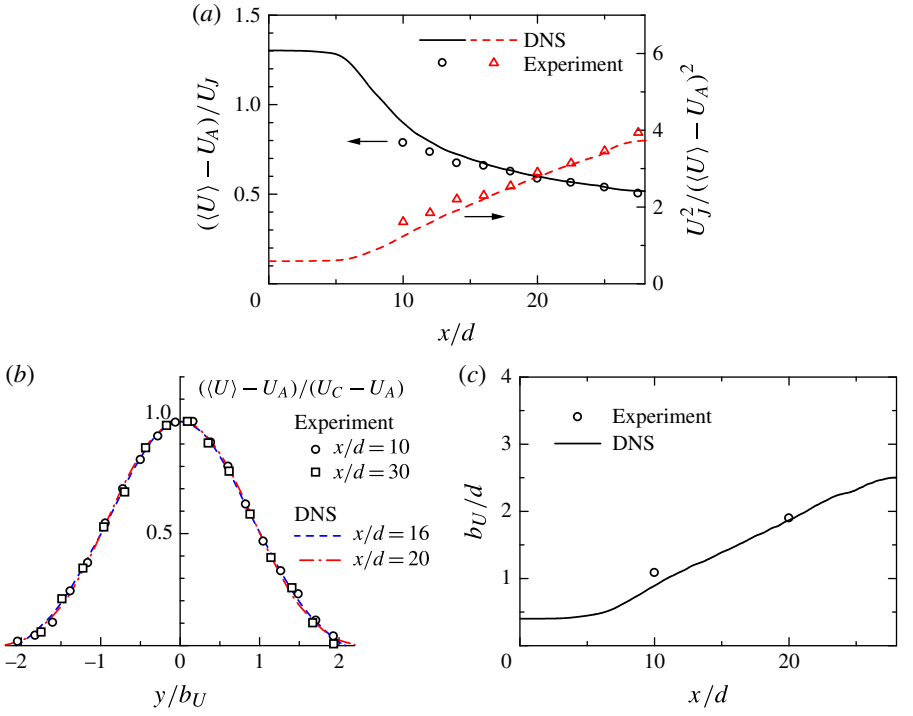


FIGURE 3. (Colour online) Comparison of mean streamwise velocity between the DNS results and the experimental results (Watanabe *et al.* 2014*b*). (*a*) Streamwise evolution of mean streamwise velocity on the jet centreline. (*b*) Lateral profiles of mean streamwise velocity. (*c*) Streamwise evolution of jet half-width based on mean streamwise velocity.

Figure 4 shows lateral profiles of the r.m.s. values of the streamwise and cross-streamwise velocity fluctuations (u_{rms} and v_{rms}) normalized by the mean streamwise velocity on the jet centreline ($U_C - U_A$). The normalized r.m.s. values in the previous experiments (Gutmark & Wygnanski 1976; Ramaprian & Chandrasekhara 1985; Watanabe *et al.* 2014*b*) and DNS (Stanley *et al.* 2002; Klein, Sadiki & Janicka 2003) are also shown in figure 4. Self-similar profiles can be observed for u_{rms} and v_{rms} obtained by the DNS, and their profiles show a similar trend to the previous studies. Thus, typical properties of the self-similar planar jet can be observed in the present DNS results.

The T/NT interface is analysed in the self-similar region. We analyse the T/NT interface detected in the region $22 \leqslant x/d \leqslant 24$, where the self-similarity can be observed without being affected by the boundary conditions. Reynolds number based on the Taylor microscale is $Re_\lambda = u_{rms}\lambda_x/\nu = 84$ at $x/d = 23$ on the jet centreline. Here, $\lambda_i = \sqrt{\langle u_i'^2\rangle/\langle(\partial u_i'/\partial x_i)^2\rangle}$ is the i-direction Taylor microscale, and $u_i' = U_i - \langle U_i\rangle$ is the instantaneous velocity fluctuation. The interface is frequently detected at $y/b_U \approx 1.8$. The computational grid sizes in the x, y and z directions are 0.82η, 1.7η and 1.7η, at $(x, y) = (23d, 1.8b_U)$, respectively, where $\eta = (\nu^3/\epsilon)^{\frac{1}{4}}$ (ϵ is the dissipation rate of turbulent kinetic energy) is the Kolmogorov microscale at $y = 0$. Here, η at $y = 0$ is used because the outer intermittency greatly affects η at $y/b_U = 1.8$. The Taylor microscale $\lambda = (\lambda_x + \lambda_y + \lambda_z)/3$ at $y = 0$ is $0.26d$ at $x/d = 22$ and is $0.29d$ at $x/d = 24$.

https://doi.org/10.1017/jfm.2014.559 Published online by Cambridge University Press

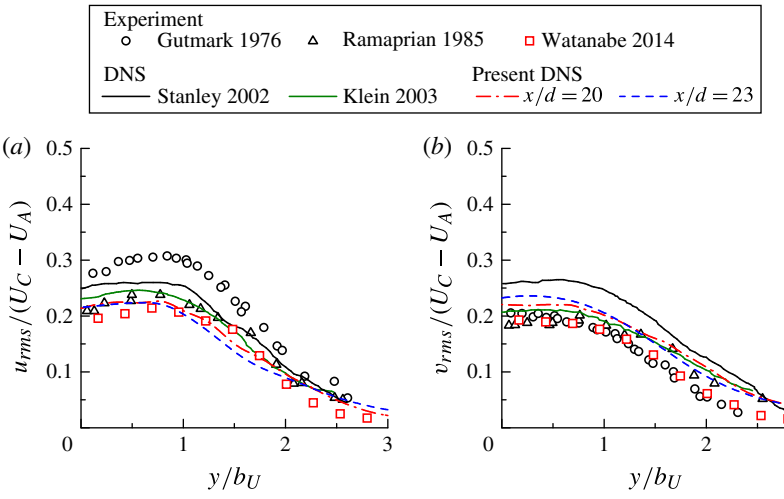


FIGURE 4. (Colour online) Lateral profiles of r.m.s. values of velocity fluctuations: (*a*) streamwise velocity; (*b*) cross-streamwise velocity. The present DNS is compared with the experiments by Gutmark & Wygnanski (1976), Ramaprian & Chandrasekhara (1985) and Watanabe *et al.* (2014*b*) and the DNS by Stanley *et al.* (2002) and Klein *et al.* (2003).

We use the enstrophy transport equation for the analysis. To investigate the error in evaluating the enstrophy transport equation, we compared the temporal derivative of enstrophy $\partial(\omega^2/2)/\partial t$ and the sum of the advection, production and viscous terms, which are here denoted by $\delta\omega_1$ and $\delta\omega_2$, respectively. Here, $\partial(\omega^2/2)/\partial t$ is estimated by using the fourth-order central difference although the DNS is conducted using the explicit/implicit hybrid scheme (Spalart *et al.* 1991). The error is estimated from $\sqrt{\langle(\delta\omega_1 - \delta\omega_2)^2\rangle/\langle{\delta\omega_2}^2\rangle}$, and is 7 % at $(x, y) = (23d, 0)$.

2.3. *T/NT interface detection method and conditional analysis near the interface*

The T/NT interface is detected by using the vorticity magnitude $|\boldsymbol{\omega}|$. According to the previous studies (Bisset, Hunt & Rogers 2002; Taveira *et al.* 2013; Watanabe *et al.* 2014*a*), the flow region where the normalized vorticity magnitude $|\boldsymbol{\omega}|b_U/U_C$ is larger than a certain threshold ω_{th} is defined as the turbulent region. Therefore, the T/NT interface is defined as the isosurface of $|\boldsymbol{\omega}|b_U/U_C = \omega_{th}$. In Taveira *et al.* (2013), the threshold ω_{th} is determined based on the dependence of the volume fraction of turbulent region Vol_T on ω_{th}. In this study, Vol_T is calculated for a wide range of ω_{th}. Because we investigate the T/NT interface around $x/d = 23$, Vol_T is calculated in the region $11L_x/16 \leqslant x \leqslant 15L_x/16$, whose volume is represented by $L_x/4 \times L_y \times L_z$. Figure 5(*a*) shows the relationship between Vol_T and ω_{th}. Although Vol_T decreases with increasing ω_{th}, there is a plateau of Vol_T for a wide range of ω_{th}. The T/NT interface location weakly depends on ω_{th} when the threshold is in the plateau-like region in figure 5(*a*) as shown in Taveira *et al.* (2013). In our analysis, $\omega_{th} = 0.3$ is used for detecting the T/NT interface. For ω_{th} smaller than 0.017, Vol_T greatly increases with decrease of ω_{th}. This is caused by numerical noise in the non-turbulent regions.

The detected T/NT interface and the vortical structures in the region $11L_x/16 \leqslant x \leqslant 15L_x/16$ are visualized in figure 5(*b*): the isosurface of $|\boldsymbol{\omega}|b_U/U_C = 0.3$, which

https://doi.org/10.1017/jfm.2014.559 Published online by Cambridge University Press

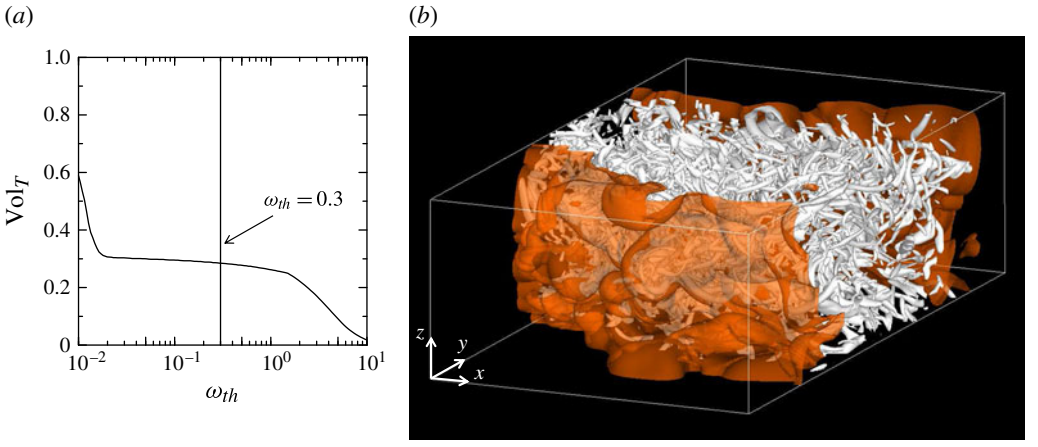


FIGURE 5. (Colour online) Detection of T/NT interface by thresholding vorticity magnitude. (*a*) Volume fraction of turbulent region in the region $11L_x/16 \leqslant x \leqslant 15L_x/16$, $-L_y/2 \leqslant y \leqslant L_y/2$ and $-L_z/2 \leqslant z \leqslant L_z/2$ as a function of the threshold ω_{th}. (*b*) Three-dimensional visualization of T/NT interface and vortical structures. Translucent orange enveloping the jet represents the T/NT interface (isosurface of $|\boldsymbol{\omega}|b_U/U_C = 0.3$). White represents the isosurface of the second invariant of the velocity gradient tensor ($Q/(U_J/d)^2 = 1$).

represents the T/NT interface, is shown by translucent orange, and the vortical structures are visualized by the isosurface (white) of the second invariant of the velocity gradient tensor, $Q = (\omega_i\omega_i - 2S_{ij}S_{ij})/4$. It is found that the vortical structures near the outflow plane are not affected by the boundary conditions, and are similar to those far from the outflow boundary. The visualization of the T/NT interface shows that the interface is convoluted and envelops the vortical structures. The convolutions of the T/NT interface are related to the large vorticity structures (da Silva *et al.* 2011).

The conditional statistics conditioned on the distance from the T/NT interface (Bisset *et al.* 2002) are used to investigate the characteristics of the T/NT interface, and are calculated by the same procedure as in Watanabe *et al.* (2014*a*). Figure 6 shows a schematic of the T/NT interface in the planar jet. The local coordinate y_I is defined for the detected interface as shown in figure 6. The location of the T/NT interface is represented by $y_I = 0$ in the local coordinate system. Here, y_I is taken to be normal to the T/NT interface and the turbulent fluid is on the side of negative y_I. The conditional average conditioned on y_I is denoted by $\langle\ \rangle_I$. Because of the strongly convoluted structures of the T/NT interface, it can face in various directions. For investigating the relationship between the interface orientation and its characteristics, the conditional statistics are calculated individually for three orientations of the T/NT interface, which are called the cross-streamwise edge, leading edge and trailing edge. Examples of these interface orientations are shown in figure 6; they are distinguished by the unit vector normal to the T/NT interface, which is defined by $\boldsymbol{n} \equiv -\nabla\omega^2/|\nabla\omega^2|$. At the cross-streamwise edge, $\boldsymbol{n}$ is parallel to the cross-streamwise direction. An interface at which $\boldsymbol{n}$ points in the streamwise direction is defined as the leading edge, whereas an interface at which $\boldsymbol{n}$ is opposite to the streamwise direction is defined as the trailing edge. It should be noted that the leading edge can be distinguished from the trailing edge because there is both mean shear and mean flow in a jet. In calculations of conditional statistics for the three interface orientations, deviations of the interface orientation within $\pm 25°$ are accepted. This criterion for

https://doi.org/10.1017/jfm.2014.559 Published online by Cambridge University Press

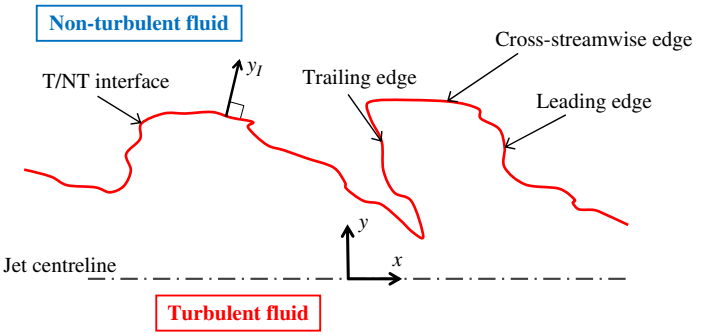


FIGURE 6. (Colour online) Schematic of T/NT interface in a jet flow and definition of interface orientation.

the interface orientation is the same as that in Bisset *et al.* (2002). For an interface detected as a cross-streamwise edge, y_I is set to be parallel to the cross-streamwise direction. Similarly, for interfaces detected as leading and trailing edges, y_I is set to be parallel to the streamwise direction. Leading and trailing edges appear with convoluted structures. Therefore, the envelop of the interface should not be used for correctly evaluating the conditional statistics near the leading and trailing edges. The conditional statistics are evaluated using the interface defined by the isosurface of vorticity norm instead of the envelope.

The conditional statistics are calculated for the turbulent and non-turbulent sides of the T/NT interface. When the conditional statistics are calculated for a T/NT interface, other interfaces can appear nearby. The characteristics of the flow field drastically vary near the T/NT interface, and the width of this variation is slightly smaller than the Taylor microscale (da Silva & Taveira 2010). Therefore, when other interfaces appear near the T/NT interface, the region within λ away from the other interfaces is not used for calculating the conditional statistics. Here, the Taylor microscale λ on the jet centreline is used, and existence of other interfaces is examined on the line of y_I. When $\omega_{th} = 0.3$ is used as the interface detection threshold, 'pockets' of non-turbulent fluid are detected in the turbulent region. These pockets are not used for calculating the conditional statistics.

3. Results and discussion

3.1. *Enstrophy transport near the T/NT interface*

Figure 7 compares the conditional average of the enstrophy $\omega^2/2$ conditioned on the distance from the T/NT interface y_I for the cross-streamwise, leading and trailing edges. The distance from the interface is normalized by λ on the jet centreline. As in many figures in this paper, the vertical broken line indicates $y_I/\lambda = -0.6$, where the conditional statistics are analysed in detail below. The enstrophy begins to increase from the T/NT interface toward the turbulent region. The conditional average of the enstrophy near the interface strongly depends on the interface orientation, being smallest near the trailing edge and largest near the cross-streamwise edge.

As shown in figure 6, the orientation of the local coordinate y_I for the leading edge is opposite to that for the trailing edge. The turbulent region near the trailing (leading) edge is downstream (upstream) of the interface. Because the enstrophy decreases in the downstream direction in the jet, the enstrophy in the turbulent region

https://doi.org/10.1017/jfm.2014.559 Published online by Cambridge University Press

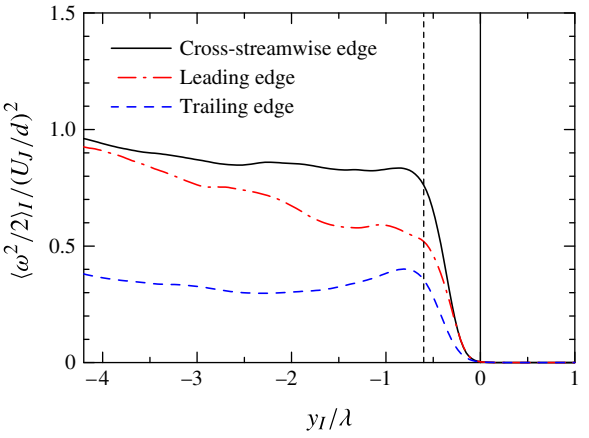


FIGURE 7. (Colour online) Conditional average of enstrophy near the cross-streamwise, leading and trailing edges.

far from the interface differs greatly between the leading and trailing edges. However, even near the T/NT interface, the conditional average of the enstrophy differs among the three interface orientations, most likely because of differences in the interface characteristics. A mean flow in a jet causes differences between the leading and trailing edges. Therefore, the difference between the leading and trailing edges, i.e. the geometrical effects on the interface characteristics, can be related to the effects of the mean flow and mean shear. The mean flow field strongly depends on the flow configuration. For example, Philip & Marusic (2012) showed that the mean flow field differs between jets and wakes in both turbulent and non-turbulent regions. Thus, the geometrical effects of the interface orientation can change depending on the flow configuration.

Figure 8 shows the conditional averages of the enstrophy production, diffusion and dissipation calculated for the three interface orientations. The conditional average of the viscous diffusion changes from negative to positive values from the turbulent region toward the T/NT interface. Thus, the enstrophy in the turbulent region is transferred toward the non-turbulent region by viscous diffusion. Viscous diffusion makes the largest contribution to the enstrophy growth near the interface. A similar conditional profile of the viscous diffusion was obtained in da Silva & Pereira (2008), Holzner *et al.* (2008) and Taveira *et al.* (2013). The trend of the conditional average of the viscous diffusion is almost independent of the interface orientation, although its is small for the trailing edge. Near the location of the negative peak of the conditionally averaged diffusion term, enstrophy is generated mainly by enstrophy production. Deep inside the turbulent region, enstrophy production almost balances enstrophy dissipation on average, similar to the case of the temporally developing jet (Taveira *et al.* 2013). However, near the T/NT interface, the conditionally averaged enstrophy production quantitatively and qualitatively depends on the interface orientation. A peak appears at $y_I/\lambda \approx -0.6$ near the cross-streamwise and leading edges. In contrast, the conditionally averaged enstrophy production decreases from the turbulent region toward the T/NT interface near the trailing edge.

Figure 9 shows the probability density function (PDF) of the enstrophy production at $y_I/\lambda = -0.6$. Large positive values of $\omega_i S_{ij} \omega_j$ arising from vortex stretching appear frequently near the cross-streamwise and leading edges, and the enstrophy

https://doi.org/10.1017/jfm.2014.559 Published online by Cambridge University Press

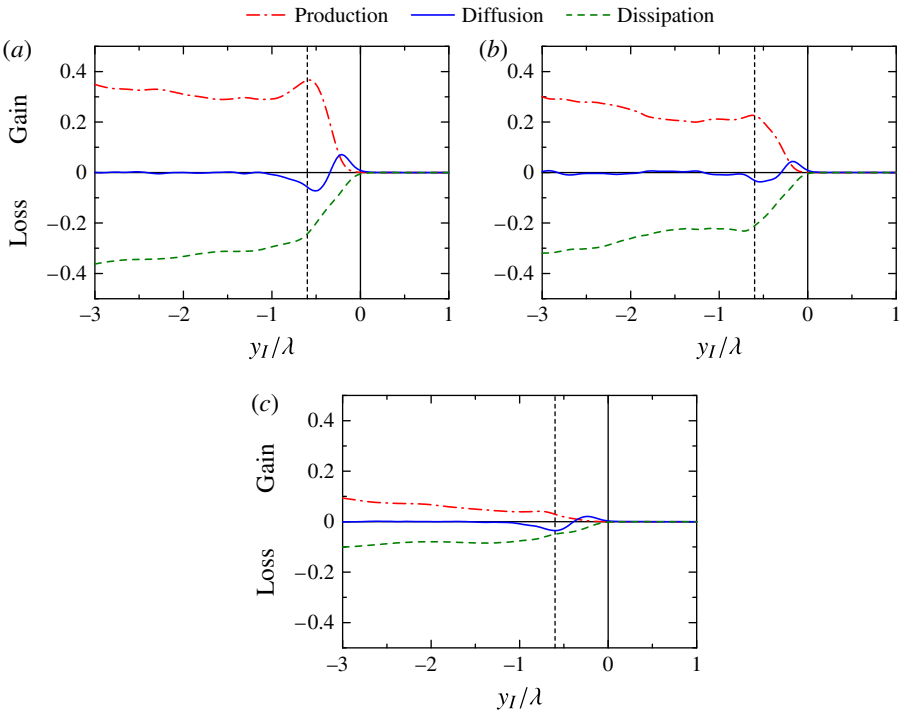


FIGURE 8. (Colour online) Conditional average of enstrophy production, diffusion and dissipation terms: (*a*) cross-streamwise edge; (*b*) leading edge; (*c*) trailing edge. The enstrophy transport equation is normalized by U_J and d.

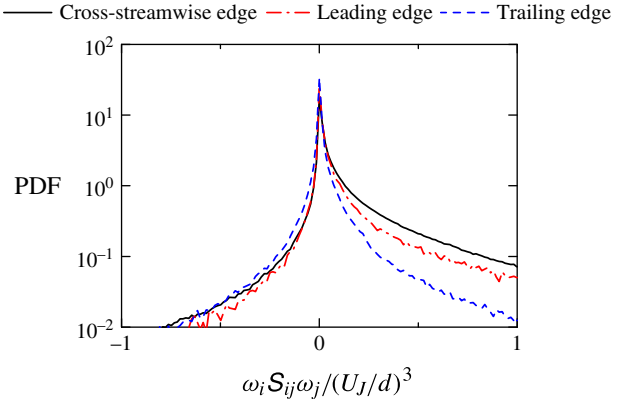


FIGURE 9. (Colour online) PDF of enstrophy production term at $y_I/\lambda = -0.6$.

production tends to be positive. Thus, enstrophy generation by vortex stretching is predominant over enstrophy reduction by vortex compression near these interfaces. In contrast, the PDF for large positive $\omega_i S_{ij} \omega_j$ is small near the trailing edge. The enstrophy production does not show a preference for positive values near the trailing edge, resulting in the small conditionally averaged enstrophy production (figure 8*c*). Figure 8 also shows that the conditionally averaged enstrophy production is largest near the cross-streamwise edge and smallest near the trailing edge. The enstrophy

https://doi.org/10.1017/jfm.2014.559 Published online by Cambridge University Press

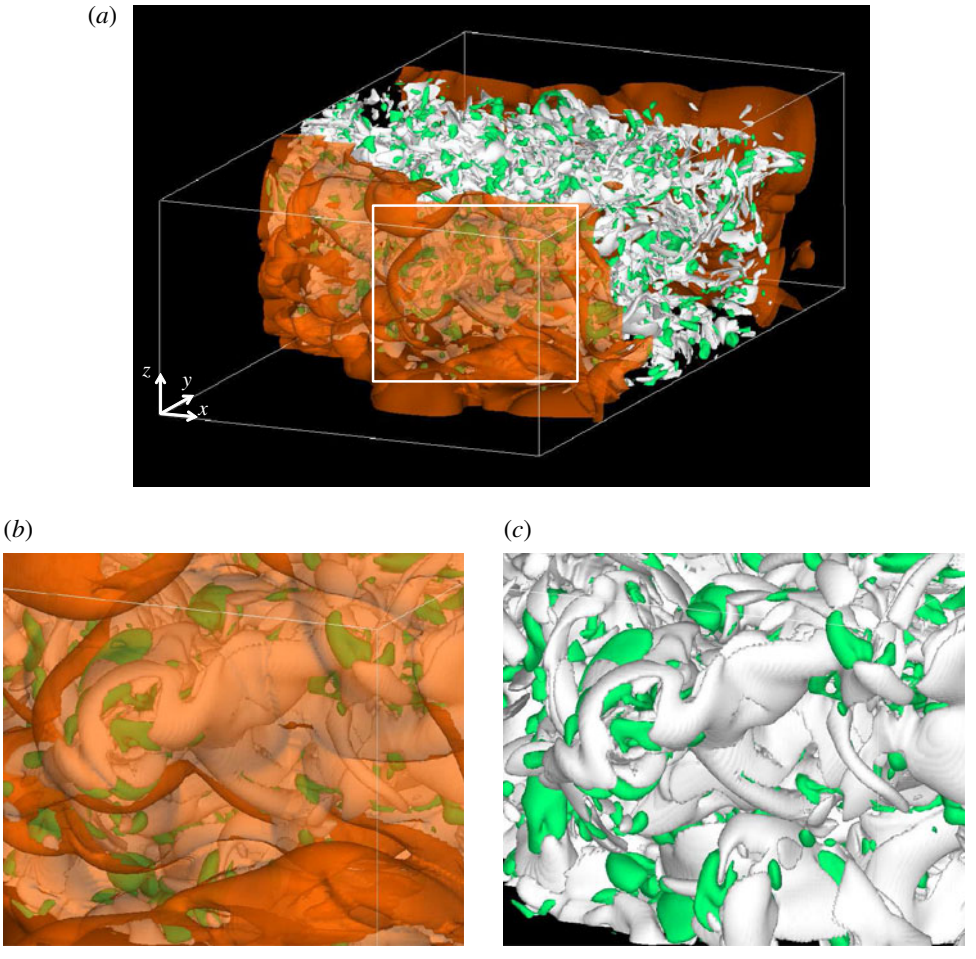


FIGURE 10. (Colour online) T/NT interface (translucent orange enveloping the jet) and isosurfaces of enstrophy production term $\omega_i S_{ij}\omega_j$. (*a*) Visualization of jet flow: white, $\omega_i S_{ij}\omega_j/(U_J/d)^3 = 3$; green, $\omega_i S_{ij}\omega_j/(U_J/d)^3 = -1.5$. (*b*) Close-up of T/NT interface (white box in *a*): white, $\omega_i S_{ij}\omega_j/(U_J/d)^3 = 0.5$; green, $\omega_i S_{ij}\omega_j/(U_J/d)^3 = -0.25$. (*c*) Close-up of T/NT interface. Only the isosurfaces of $\omega_i S_{ij}\omega_j$ are visualized; they are the same as in (*b*).

production $\omega_i S_{ij}\omega_j$ is proportional to the enstrophy $\omega^2/2$, as shown in (1.2). One of the reasons why $\omega_i S_{ij}\omega_j$ depends on the interface orientation is that the values of the enstrophy differ among the three orientations even near the T/NT interface (figure 7). However, a comparison of the enstrophy (figure 7) and the enstrophy production (figure 8) shows that the interface orientation has a more significant influence on the enstrophy production than on the enstrophy. Therefore, the enstrophy production in (1.2) implies that the strain-rate eigenvalues s_i and the relationship between their eigenvectors $\boldsymbol{e}_i$ and the vorticity vector $\hat{\boldsymbol{\omega}}$ also depend on the interface orientation.

Figure 10(*a*) shows the T/NT interface and isosurfaces of the enstrophy production $\omega_i S_{ij}\omega_j$. The vortex stretching regions are visualized by the isosurfaces of positive enstrophy production (white), and the vortex compression regions are visualized by those of negative enstrophy production (green). A close-up of the T/NT interface is shown in figure 10(*b*,*c*) to illustrate the topological structures of vortex stretching

https://doi.org/10.1017/jfm.2014.559 Published online by Cambridge University Press

and compression near the interface. The vortex stretching region near the interface shows sheet-like structures, and small spots of vortex compression can be observed near the interface. The topological structures of vortex stretching and compression near the T/NT interface are similar to those in the turbulent core region visualized in figure 10(*a*) and observed experimentally in an axisymmetric jet (Buxton & Ganapathisubramani 2010).

3.2. *Invariants of the velocity gradient tensor and the rate-of-strain tensor*

The invariants of the velocity gradient tensor and rate-of-strain tensor have been investigated in various turbulent flows (Soria *et al.* 1994; Blackburn, Mansour & Cantwell 1996; Ooi *et al.* 1999; Zhou *et al.* 2014). The invariants near the T/NT interface were first studied by da Silva & Pereira (2008), who revealed the dynamics, geometry and topology of the local flow field. However, they did not consider the interface orientation. In this study, the invariants of the velocity gradient tensor and rate-of-strain tensor are analysed for the three interface orientations.

The eigenvalues Λ_{Ai} ($i = 1$–3) of the velocity gradient tensor $A_{ij} = \partial U_i/\partial x_j$ satisfy the characteristic equation

$$\Lambda_{Ai}^3 + P\Lambda_{Ai}^2 + Q\Lambda_{Ai} + R = 0, \tag{3.1}$$

where P, Q and R are the first, second and third invariants of A_{ij}, respectively. In an incompressible flow, $P = -A_{ii} = 0$. The second invariant Q and the third invariant R are written as

$$Q = \tfrac{1}{4}\left(\omega_i\omega_i - 2S_{ij}S_{ij}\right), \tag{3.2}$$

$$R = -\tfrac{1}{3}\left(S_{ij}S_{jk}S_{ki} + \tfrac{3}{4}\omega_i\omega_j S_{ij}\right). \tag{3.3}$$

The discriminant of A_{ij} is given by

$$D_A = \tfrac{27}{4}R^2 + Q^3. \tag{3.4}$$

The joint PDF of Q and R is used to classify the topological structure of the local flow field (Davidson 2004; da Silva & Pereira 2008). When $D_A > 0$ (i.e. $Q > -3(R^2/4)^{\frac{1}{3}}$), a negative R implies vortex stretching, whereas a positive R implies vortex compression. On the other hand, when $D_A < 0$ (i.e. $Q < -3(R^2/4)^{\frac{1}{3}}$), a negative R implies a region of axial strain (tube-like structure), whereas a positive R implies a region of biaxial strain (sheet-like structure).

The invariants of the rate-of-strain tensor S_{ij} are written as

$$Q_S = -\tfrac{1}{2}S_{ij}S_{ij}, \tag{3.5}$$

$$R_S = -\tfrac{1}{3}S_{ij}S_{jk}S_{ki}. \tag{3.6}$$

By using the eigenvalues of the rate-of-strain tensor s_i (here, $s_1 \geqslant s_2 \geqslant s_3$), R_S is represented by $R_S = -s_1s_2s_3$. In an incompressible flow, $s_1 + s_2 + s_3 = 0$. When a is defined as $a = s_2/s_1$, the following equation is used to classify the flow geometry:

$$R_S = (-Q_S)^{\frac{3}{2}}a(1+a)(1+a+a^2)^{-\frac{3}{2}}. \tag{3.7}$$

The flow geometry is indicated by the lines of (3.7) corresponding to $s_1{:}s_2{:}s_3 =$ 2:−1:−1 (axisymmetric contraction), 1:0:−1 (two-dimensional flow), 3:1:−4 (biaxial stretching) and 1:1:−2 (axial stretching) (da Silva & Pereira 2008). The joint PDF

https://doi.org/10.1017/jfm.2014.559 Published online by Cambridge University Press

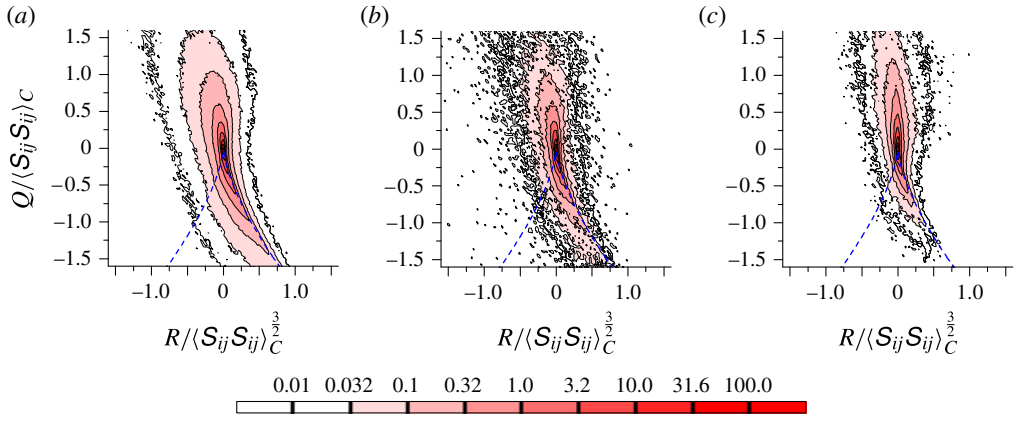


FIGURE 11. (Colour online) Joint PDF of Q and R near the T/NT interface ($y_I/\lambda = -0.6$): (*a*) cross-streamwise edge; (*b*) leading edge; (*c*) trailing edge. Blue broken line shows $D_A = 0$ ($Q = -3(R^2/4)^{\frac{1}{3}}$).

of Q_S and R_S is used with (3.7) to analyse the flow geometry. Furthermore, because $R_S = -s_1 s_2 s_3$, the flow structure corresponding to negative R_S is tube-like, whereas that corresponding to positive R_S is sheet-like.

Figure 11 shows the joint PDF of Q and R at $y_I/\lambda = -0.6$, which is in the turbulent region. The invariants are normalized by the mean strain product on the jet centreline, which is denoted by $\langle S_{ij}S_{ij}\rangle_C$. When $D_A < 0$ ($Q < -3(R^2/4)^{\frac{1}{3}}$), R tends to be positive near these three interfaces, and the joint PDF indicates that sheet-like structures exist in the turbulent region near them. However, the tail of the joint PDF for negative Q and positive R is short near the trailing edge. When $D_A > 0$, R tends to be negative near the cross-streamwise and leading edges, as shown in figure 11(*a*,*b*). The region with $D_A > 0$ and $R < 0$ is characterized by strong vortex stretching (Buxton & Ganapathisubramani 2010; Taveira *et al.* 2013). In contrast, the joint PDF near the trailing edge (figure 11(*c*) maps not only negative R but also positive R when $D_A > 0$. The region with $D_A > 0$ and $R > 0$ is characterized by vortex compression, which reduces the enstrophy. Thus, the joint PDF of Q and R also indicates that the enstrophy production is small in the turbulent region near the trailing edge.

Figure 12 shows the joint PDF of Q and R at the interface ($y_I/\lambda = 0$). Because the T/NT interface is defined as the isosurface of small enstrophy values, the joint PDF maps negative Q. At the cross-streamwise and leading edges, the joint PDF of Q and R preferentially maps near the line of $D_A = 0$ in the region with $R > 0$. A similar trend was observed in the joint PDF obtained for a temporally developing jet (da Silva & Pereira 2008). In contrast, the ridge of the joint PDF does not align with $D_A = 0$ at the trailing edge but with the line of $R = 0$, and it maps both positive and negative R. Because of the small enstrophy at the T/NT interface, Q and R are approximated by $-S_{ij}S_{ij}/2$ and $-S_{ij}S_{jk}S_{ki}/3$, respectively. Therefore, the difference in the joint PDF of Q and R at the T/NT interface among the three interface orientations is attributed to the strain field.

Figure 13 shows the joint PDF of Q_S and R_S at $y_I/\lambda = -0.6$. In the turbulent region near the T/NT interface, it maps mainly $Q_S < 0$ and $R_S > 0$. Near the cross-streamwise and leading edges, a large probability appears between the lines of (3.7) corresponding to $s_1{:}s_2{:}s_3 = 3{:}1{:}-4$ and $1{:}1{:}-2$. Thus, axial or biaxial stretching appears frequently near the cross-streamwise and leading edges. On the other hand, near the trailing edge,

https://doi.org/10.1017/jfm.2014.559 Published online by Cambridge University Press

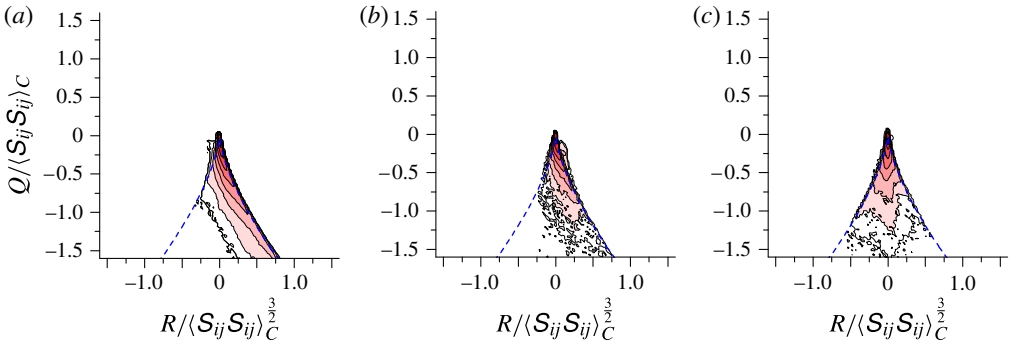


FIGURE 12. (Colour online) Joint PDF of Q and R at the T/NT interface ($y_I/\lambda = 0$): (*a*) cross-streamwise edge; (*b*) leading edge; (*c*) trailing edge. Blue broken line shows $D_A = 0$ ($Q = -3(R^2/4)^{\frac{1}{3}}$). Colour contours are the same as in figure 11.

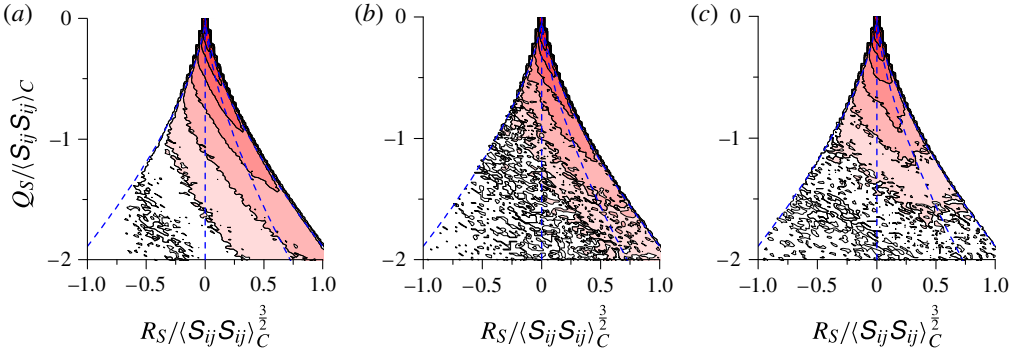


FIGURE 13. (Colour online) Joint PDF of Q_S and R_S near the T/NT interface ($y_I/\lambda = -0.6$): (*a*) cross-streamwise edge; (*b*) leading edge; (*c*) trailing edge. The four lines of (3.7) corresponding to $s_1{:}s_2{:}s_3 = 2{:}-1{:}-1$, $1{:}0{:}-1$, $3{:}1{:}-4$ and $1{:}1{:}-2$ are shown by blue broken lines in order from left to right. Colour contours are the same as in figure 11.

the ridge of the joint PDF appears on the line of (3.7) corresponding to $s_1{:}s_2{:}s_3 = 3{:}1{:}-4$. A large positive R_S appears at the trailing edge less frequently than at the cross-streamwise and leading edges.

Figure 14 shows the joint PDF of Q_S and R_S at the T/NT interface ($y_I/\lambda = 0$). At the interface, the ratios $(\langle s_1\rangle_I{:}\langle s_2\rangle_I{:}\langle s_3\rangle_I)$ are (4, 1, −5), (4, 1, −5) and (9, 1, −10) for the cross-streamwise, leading and trailing edges, respectively. The large $\langle s_1\rangle_I$ and $\langle s_3\rangle_I$ relative to $\langle s_2\rangle_I$ for the trailing edge are caused by the small $\langle s_2\rangle_I$, which is almost 0. At the cross-streamwise and leading edges, the shape of the joint PDF of Q_S and R_S is similar to that in the turbulent region. The preference for positive R_S was also observed at the interface in the temporally developing jet (da Silva & Pereira 2008). However, the joint PDF of Q_S and R_S at the trailing edge differs greatly from that in the turbulent region, and the large probability appears on the line of (3.7) corresponding to $s_1{:}s_2{:}s_3 = 1{:}0{:}-1$. Note that the joint PDF preferentially maps negative R_S at the trailing edge rather than positive R_S. This implies that the flow field at the trailing edge is characterized by a tube-like structure. At the cross-streamwise and leading edges (figure 14*a*,*b*) and the turbulent region near the interface (figure 13), the joint PDF of Q_S and R_S preferentially maps positive R_S, indicating that the flow

https://doi.org/10.1017/jfm.2014.559 Published online by Cambridge University Press

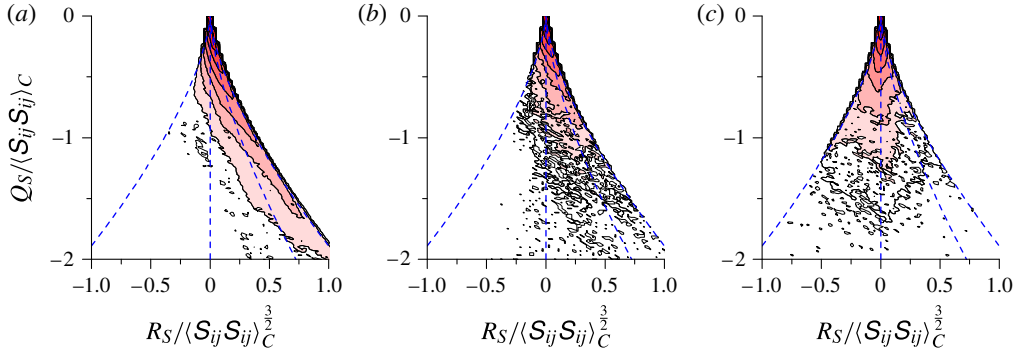


FIGURE 14. (Colour online) Joint PDF of Q_S and R_S at the T/NT interface ($y_I/\lambda = 0$): (*a*) cross-streamwise edge; (*b*) leading edge; (*c*) trailing edge. Blue broken lines and colour contours are the same as in figure 13.

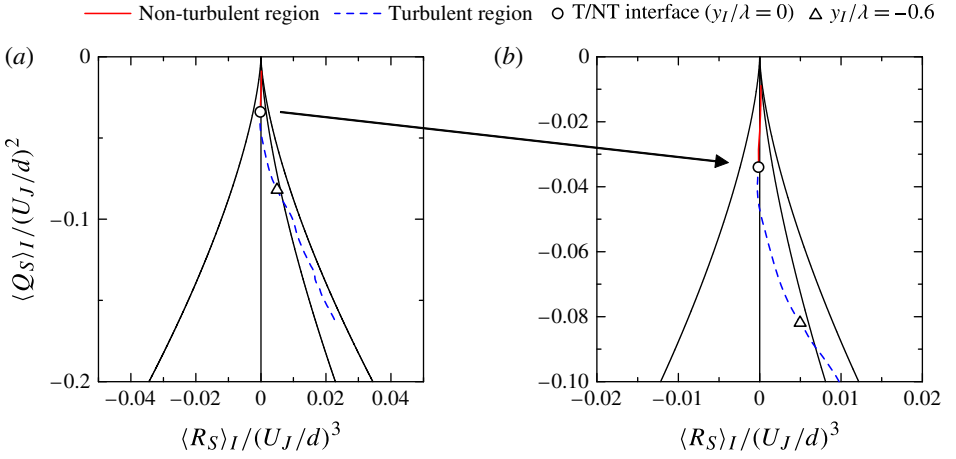


FIGURE 15. (Colour online) (*a*) Mean trajectory of Q_S and R_S in the phase map near the trailing edge from $y_I/\lambda = 1$ to -3. (*b*) A close-up of the trajectory near the interface. Circle and triangle indicate locations of $y_I/\lambda = 0$ and -0.6, respectively. The four lines of (3.7) corresponding to $s_1{:}s_2{:}s_3 = 2{:}-1{:}-1$, $1{:}0{:}-1$, $3{:}1{:}-4$ and $1{:}1{:}-2$ are shown by black solid lines in order from left to right.

field is characterized by sheet-like structures. The joint PDF of Q_S and R_S in the turbulent region differs slightly between the trailing edge and the cross-streamwise and leading edges (figure 13). This difference can be considered as the imprint of the large difference in the flow structure at the T/NT interface (figure 14).

Figure 15 shows the mean trajectory of Q_S and R_S near the trailing edge. The mean trajectory in the non-turbulent region appears on the line for $s_1{:}s_2{:}s_3 = 1{:}0{:}-1$. Even in the turbulent region near the interface, the mean flow topology is $1{:}0{:}-1$. Beyond $y_I/\lambda \approx -0.6$, the mean trajectory moves to the region between $3{:}1{:}-4$ and $1{:}1{:}-2$. We also found that the mean trajectory in the non-turbulent region near the cross-streamwise and leading edges appears near the line for $s_1{:}s_2{:}s_3 = 3{:}1{:}-4$, similar to da Silva & Pereira (2008). At the trailing edge, the joint PDFs also differ greatly from those shown in da Silva & Pereira (2008). These characteristics near the trailing

https://doi.org/10.1017/jfm.2014.559 Published online by Cambridge University Press

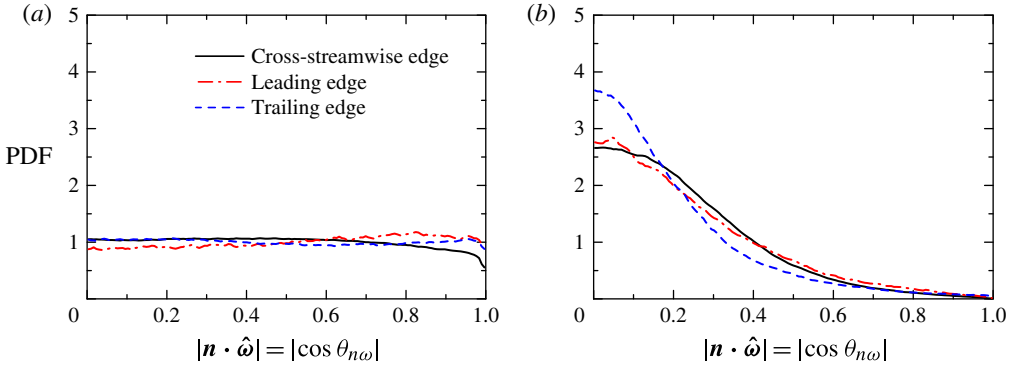


FIGURE 16. (Colour online) PDF of cosine of alignment angle between the unit normal vector to the T/NT interface ($\boldsymbol{n}$) and the vorticity vector ($\hat{\boldsymbol{\omega}}$): (*a*) deep inside the turbulent region ($y_I/\lambda = -4$); (*b*) near the T/NT interface ($y_I/\lambda = -0.6$).

edge are veiled by those of the other interface orientations when one calculates the statistics without distinguishing the interface orientations, as in da Silva & Pereira (2008). They suggested that the irrotational dissipation near the interface might arise from the instantaneous pure shear motions induced by the large-scale motions, although they also raised the possibility that it is caused by small-scale processes near the interface. Thus, the large-scale motions are related to the strain field in the non-turbulent regions. The large-scale motions that dominate the non-turbulent fluid depend on the interface orientation. For example, engulfed non-turbulent fluid often appears between the leading and trailing edges. The mean flow also causes the difference in the velocity field near the interface between the leading and trailing edges, as discussed below. Therefore, the different characteristics of Q_S and R_S for the different interface orientations might be caused by the large-scale motions near the interface.

3.3. *Alignment of T/NT interface, vorticity vector and strain-rate eigenvectors*

We investigate the alignment of the unit normal vector of the interface $\boldsymbol{n}$, the vorticity vector $\hat{\boldsymbol{\omega}}$ and the strain-rate eigenvectors $\boldsymbol{e}_i$ using the PDF of the cosine of the alignment angles between two of these three vectors. Because these three vectors are unit vectors, the cosine of the alignment angle can be obtained by taking an inner product.

First, we investigate the alignment angle between $\boldsymbol{n}$ and $\hat{\boldsymbol{\omega}}$ ($\theta_{n\omega}$). Figure 16 compares the PDFs of the cosine of $\theta_{n\omega}$ deep inside the turbulent region ($y_I/\lambda = -4$) and near the T/NT interface ($y_I/\lambda = -0.6$). Deep inside the turbulent region, the PDF of $|\cos\theta_{n\omega}|$ is almost flat for all three interface orientations. Thus, the vorticity vector is arbitrarily oriented. In contrast, near the T/NT interface, the PDF is large for $|\cos\theta_{n\omega}| \approx 0$ and small for $|\cos\theta_{n\omega}| \approx 1$. The orientation of the vorticity vector is confined near the T/NT interface, so the vorticity vector is perpendicular to $\boldsymbol{n}$. Therefore, the vorticity tends to be tangential to the T/NT interface. The tendency toward perpendicular alignment between $\boldsymbol{n}$ and $\hat{\boldsymbol{\omega}}$ is independent of the interface orientation.

Figure 17 shows the PDF of the cosine of the alignment angle between $\boldsymbol{n}$ and $\boldsymbol{e}_i(\theta_{ne_i})$ at $y_I/\lambda = -0.6$. The PDF of $|\cos\theta_{ne_2}|$ is large for $|\cos\theta_{ne_2}| \approx 0$, and the intermediate strain-rate eigenvector $\boldsymbol{e}_2$ tends to be perpendicular to $\boldsymbol{n}$ (figure 17*b*). The PDF of $|\cos\theta_{ne_2}|$ shows a similar profile for all three interface orientations.

https://doi.org/10.1017/jfm.2014.559 Published online by Cambridge University Press

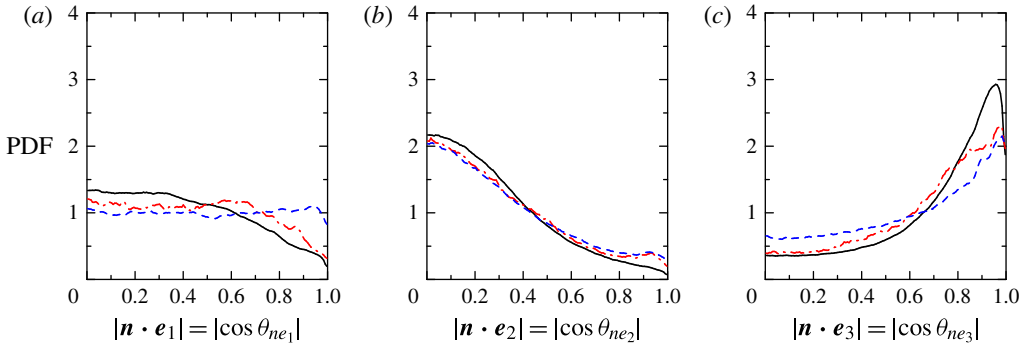


FIGURE 17. (Colour online) PDF of cosine of alignment angle between the normal vector to the T/NT interface ($\boldsymbol{n}$) and the eigenvectors of the rate-of-strain tensor ($\boldsymbol{e}_i$) near the T/NT interface ($y_I/\lambda = -0.6$). Lines are same as in figure 16. (*a*) Extensive strain-rate eigenvector $\boldsymbol{e}_1$; (*b*) intermediate strain-rate eigenvector $\boldsymbol{e}_2$; (*c*) compressive strain-rate eigenvector $\boldsymbol{e}_3$.

Thus, $\boldsymbol{e}_2$ near the T/NT interface shows a preference for tangential alignment with the interface. The PDF of $|\cos\theta_{\boldsymbol{ne}_1}|$ depends on the interface orientation (figure 17*a*). Near the cross-streamwise and leading edges, the PDF of $|\cos\theta_{\boldsymbol{ne}_1}|$ is small for $|\cos\theta_{\boldsymbol{ne}_1}| \approx 1$, and the extensive strain-rate eigenvector $\boldsymbol{e}_1$ tends not to align with $\boldsymbol{n}$. However, the PDF of $|\cos\theta_{\boldsymbol{ne}_1}|$ is almost flat near the trailing edge, and an arbitrary alignment between $\boldsymbol{n}$ and $\boldsymbol{e}_1$ appears. Figure 17(*c*) shows that the PDF of $|\cos\theta_{\boldsymbol{ne}_3}|$ is large for $|\cos\theta_{\boldsymbol{ne}_3}| \approx 1$. The compressive strain-rate eigenvector $\boldsymbol{e}_3$ shows a preference for parallel alignment with $\boldsymbol{n}$, and vortex compression by s_3 acts in the direction normal to the T/NT interface. Near the trailing edge, the PDF of $|\cos\theta_{\boldsymbol{ne}_3}|$ for small $|\cos\theta_{\boldsymbol{ne}_3}|$ is larger than those near the cross-streamwise and leading edges. Thus, vortex compression by s_3 often acts in the direction tangential to the trailing edge.

Because the presence of the T/NT interface confines the orientation of the vorticity to the direction tangential to the interface, the dependence of the strain-rate eigenvectors on the interface orientation is expected to affect the alignment between the vorticity and strain-rate eigenvectors, which is important for enstrophy production. Figure 18 shows the PDF of the cosine of the alignment angle between $\hat{\boldsymbol{\omega}}$ and $\boldsymbol{e}_i(\theta_{\boldsymbol{\omega e}_i})$ on the jet centreline. The PDF of $|\cos\theta_{\boldsymbol{\omega e}_1}|$ is almost flat, and $\boldsymbol{e}_1$ aligns arbitrarily with the vorticity. Further, $\boldsymbol{e}_2$ preferentially aligns with the vorticity vector, whereas $\boldsymbol{e}_3$ tends to be perpendicular to the vorticity vector. Similar profiles of the PDF of $|\cos\theta_{\boldsymbol{\omega e}_i}|$ have been observed in various turbulent flows (Ashurst *et al.* 1987; Jiménez 1992; Tanahashi *et al.* 2001; Buxton & Ganapathisubramani 2010). Figure 19 compares the PDF of $|\cos\theta_{\boldsymbol{\omega e}_i}|$ near the T/NT interface ($y_I/\lambda = -0.6$) at the cross-streamwise, leading and trailing edges. The PDF of $|\cos\theta_{\boldsymbol{\omega e}_1}|$ in figure 19(*a*) is slightly larger than one for $|\cos\theta_{\boldsymbol{\omega e}_1}| \approx 0$. However, $\boldsymbol{e}_1$ aligns almost arbitrarily with the vorticity vector. In addition, the alignment between $\hat{\boldsymbol{\omega}}$ and $\boldsymbol{e}_1$ is independent of the interface orientation. The PDF of $|\cos\theta_{\boldsymbol{\omega e}_2}|$ near the T/NT interface (figure 19*b*) is very similar to that on the jet centreline (figure 18), and $\boldsymbol{e}_2$ preferentially aligns with the vorticity vector. Therefore, vortex stretching or compression by s_2 effectively acts on the vorticity near the T/NT interface because $|\hat{\boldsymbol{\omega}}\cdot\boldsymbol{e}_2| \approx 1$. The alignments between $\hat{\boldsymbol{\omega}}$ and $\boldsymbol{e}_1$ and $\boldsymbol{e}_2$ are almost independent of the interface orientation. In contrast, the alignment between $\hat{\boldsymbol{\omega}}$ and $\boldsymbol{e}_3$ strongly depends on the interface orientation (figure 19*c*). Here, $\boldsymbol{e}_3$ tends to be perpendicular to the vorticity vector. The peak value of the PDF

https://doi.org/10.1017/jfm.2014.559 Published online by Cambridge University Press

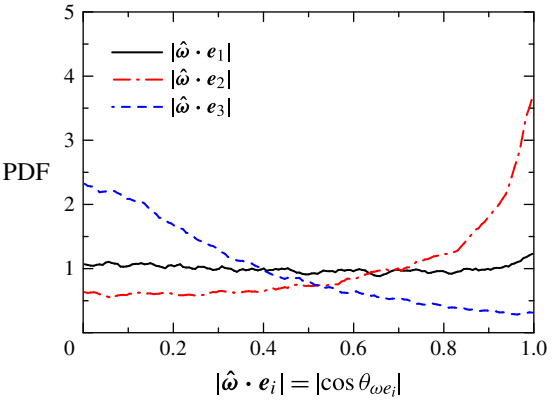


FIGURE 18. (Colour online) PDF of cosine of alignment angle between the vorticity vector ($\hat{\boldsymbol{\omega}}$) and the eigenvectors of the rate-of-strain tensor ($\boldsymbol{e}_i$) on the jet centreline.

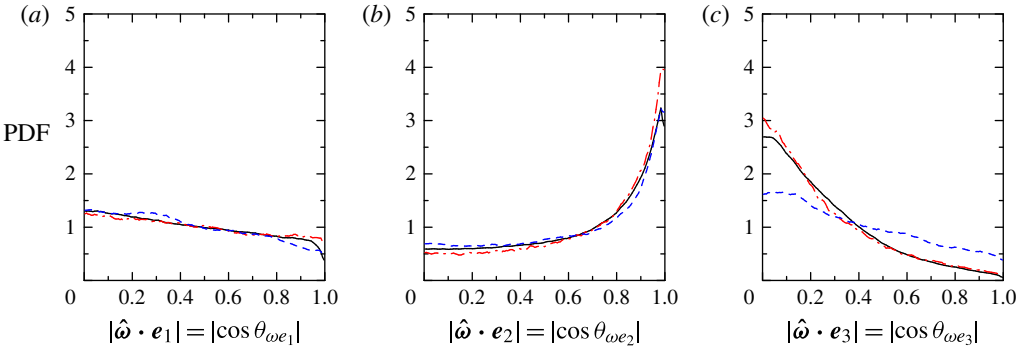


FIGURE 19. (Colour online) PDF of cosine of alignment angle between the eigenvectors of the rate-of-strain tensor ($\boldsymbol{e}_i$) and the vorticity vector ($\hat{\boldsymbol{\omega}}$) near the T/NT interface ($y_I/\lambda = -0.6$). Lines are same as in figure 16. (*a*) Extensive strain-rate eigenvector $\boldsymbol{e}_1$; (*b*) intermediate strain-rate eigenvector $\boldsymbol{e}_2$; (*c*) compressive strain-rate eigenvector $\boldsymbol{e}_3$.

for $|\cos\theta_{\omega e_3}| \approx 0$ near the cross-streamwise and leading edges is larger than those deep inside the turbulent region (figure 18) and near the trailing edge. A comparison of the PDF of $|\cos\theta_{\omega e_3}|$ deep inside the turbulent region (figure 18) and near the T/NT interface (figure 19*c*) shows that the perpendicular alignment between $\hat{\boldsymbol{\omega}}$ and $\boldsymbol{e}_3$ appears more clearly near the cross-streamwise and leading edges. Near the trailing edge, $\boldsymbol{e}_3$ often aligns with $\hat{\boldsymbol{\omega}}$, unlike the case deep inside the turbulent region and near the cross-streamwise and leading edges. Because of the tendency toward perpendicular alignment between $\boldsymbol{\omega}$ and $\boldsymbol{e}_3$ near the cross-streamwise and leading edges, the compressive strain due to s_3 acts ineffectively on the vorticity. However, the vorticity near the trailing edge is strongly affected by the compressive strain due to s_3 because of the parallel alignment between $\boldsymbol{\omega}$ and $\boldsymbol{e}_3$.

3.4. *Eigenvalues of rate-of-strain tensor and its contribution to enstrophy production*

The rate-of-strain tensor affects the enstrophy production $\omega_i S_{ij}\omega_j = \omega^2 s_i(\hat{\boldsymbol{\omega}}\cdot\boldsymbol{e}_i)^2$ through two factors. One is the alignment between the vorticity and strain-rate

https://doi.org/10.1017/jfm.2014.559 Published online by Cambridge University Press

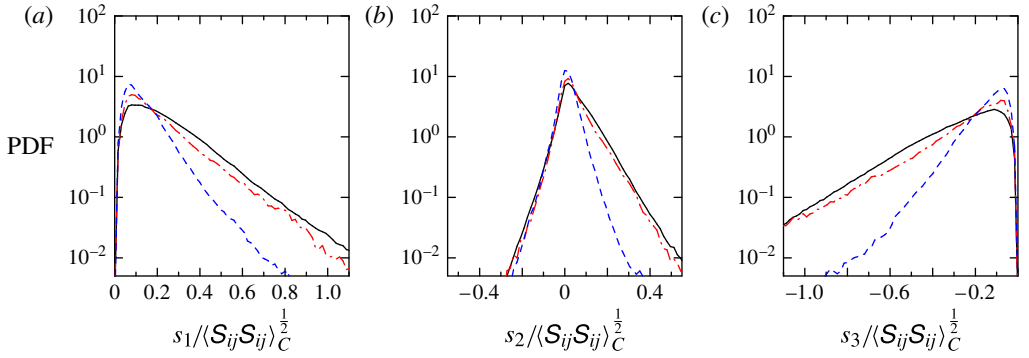


FIGURE 20. (Colour online) PDF of strain-rate eigenvalues near the T/NT interface ($y_I/\lambda = -0.6$). Lines are same as in figure 16. The strain-rate eigenvalues are normalized by the mean strain product on the jet centreline. (*a*) Extensive strain-rate eigenvalue s_1; (*b*) intermediate strain-rate eigenvalue s_2; (*c*) compressive strain-rate eigenvalue s_3.

eigenvectors, which is discussed above. The other is the intensity of vortex stretching or compression represented by the strain-rate eigenvalues s_i. Figure 20 shows the PDF of the strain-rate eigenvalues s_i at $y_I/\lambda = -0.6$. Figure 20(*a*) shows that s_1 tends to be large near the cross-streamwise and leading edges and small near the trailing edge. Therefore, strong vortex stretching by s_1 appears frequently near the cross-streamwise and leading edges. The PDF is almost symmetric about $s_2 = 0$ near the trailing edge (figure 20*b*), and both vortex stretching and compression occur due to s_2. In contrast, s_2 shows a preference for positive values near the cross-streamwise and leading edges. The positive value of s_2 is small compared with that of s_1, and s_2 does not greatly amplify the enstrophy. However, s_2 is important for enstrophy production because the strain by s_2 effectively acts on the vorticity in turbulent flows owing to the parallel alignment between its eigenvector and the vorticity vector. Because $s_1 + s_2 + s_3 = 0$ in an incompressible flow, a large negative s_3 appears frequently near the cross-streamwise and leading edges (figure 20*c*), where s_1 and s_2 show a preference for large positive values. In contrast, the magnitude of s_3 near the trailing edge is small. Thus, both strong vortex stretching and compression act on the vorticity near the cross-streamwise and leading edges, whereas the vorticity near the trailing edge is under weak vortex stretching and compression represented by small $|s_i|$.

The enstrophy production can be decomposed into the contributions from three eigenvalues, as shown in (1.2). To compare the three interface orientations, which are characterized by different levels of enstrophy, we investigate the enstrophy production divided by ω^2:

$$\omega_i S_{ij} \omega_j / \omega^2 = s_i (\hat{\boldsymbol{\omega}} \cdot \boldsymbol{e}_i)^2. \tag{3.8}$$

Figure 21 shows the PDF of the three components of $s_i(\hat{\boldsymbol{\omega}} \cdot \boldsymbol{e}_i)^2$ at $y_I/\lambda = -0.6$. The enstrophy production due to the extensive strain-rate eigenvalue, $s_1(\hat{\boldsymbol{\omega}} \cdot \boldsymbol{e}_1)^2$, tends to be large near the cross-streamwise and leading edges because strong vortex stretching, which is represented by large s_1, acts on the vorticity near these two interfaces (figure 20*a*). On the other hand, s_2 makes both positive and negative contributions to the enstrophy production. Because the alignment angle between $\hat{\boldsymbol{\omega}}$ and $\boldsymbol{e}_2$ is almost independent of the interface orientation (figure 19*b*), the PDF of $s_2(\hat{\boldsymbol{\omega}} \cdot \boldsymbol{e}_2)^2$ differs because s_2 depends on the interface orientation. Further, $\boldsymbol{e}_2$ shows a preference for parallel alignment with $\hat{\boldsymbol{\omega}}$, and the strain due to s_2 acts effectively on

https://doi.org/10.1017/jfm.2014.559 Published online by Cambridge University Press

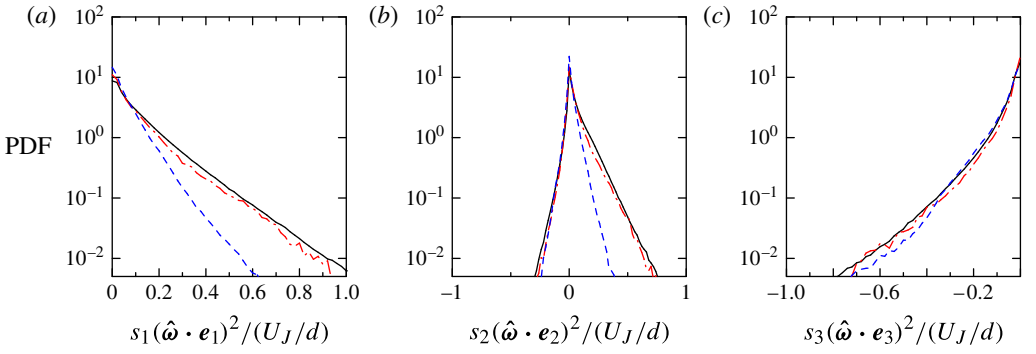


FIGURE 21. (Colour online) PDF of enstrophy production term normalized by the enstrophy near the T/NT interface ($y_I/\lambda = -0.6$). Contributions of three eigenvalues are shown separately: (*a*) extensive strain-rate eigenvector; (*b*) intermediate strain-rate eigenvector; (*c*) compressive strain-rate eigenvector. Lines are same as in figure 16.

the vorticity. Therefore, as shown in figure 21(*a*,*b*), the enstrophy generation by s_2 is comparable to $s_1(\hat{\boldsymbol{\omega}}\cdot\boldsymbol{e}_1)^2$, although s_2 is smaller than s_1. The enstrophy generation by s_1 and s_2 is small near the trailing edge because of the small eigenvalues. The PDF of $s_3(\hat{\boldsymbol{\omega}}\cdot\boldsymbol{e}_3)^2$ is almost independent of the interface orientation (figure 21*c*). Strong vortex compression by s_3 acts on the vorticity near the cross-streamwise and leading edges because of the large negative s_3. However, because $\boldsymbol{e}_3$ tends to be perpendicular to the vorticity vector, vortex compression by s_3 acts ineffectively on the vorticity near the cross-streamwise and leading edges. In contrast, $\boldsymbol{e}_3$ is oriented parallel to the vorticity vector more frequently near the trailing edge than near the cross-streamwise and leading edges. Although the vorticity near the trailing edge is under weak vortex compression by small $|s_3|$, it effectively acts on the vorticity near the trailing edge, resulting in the large negative $s_3(\hat{\boldsymbol{\omega}}\cdot\boldsymbol{e}_3)^2$. Thus, the small enstrophy production near the trailing edge in figure 9 is caused by the small s_1 and s_2 and effective vortex compression by s_3.

The vorticity vector and strain-rate eigenvectors are confined by the presence of the T/NT interface, and the strain-rate eigenvalues also change depending on the interface orientation. These results show that vortex stretching and compression significantly depend on the characteristics of the T/NT interface. We also confirmed that these characteristics of the alignments and enstrophy production term are observed at $y_I/\lambda = -0.3$, which is closer to the interface than $y_I/\lambda = -0.6$.

3.5. *Velocity field near the T/NT interface*

To investigate the factors affecting vortex stretching and compression near the interface, we analyse the relationship between the enstrophy production and the velocity field in this region. In particular, we focus on the motion of the turbulent fluid normal to the T/NT interface. Figure 22 shows the relationship between the velocity of the T/NT interface and the velocity of turbulent fluid in the direction normal to the interface. Here, we consider the turbulent fluid on the line normal to the interface to analyse the conditional statistics conditioned on the local coordinate y_I. The velocity of the interface, $\boldsymbol{U}^I$, can be divided into the local entrainment velocity $\boldsymbol{V}^P$ and the velocity of the fluid in which the interface is located:

$$\boldsymbol{U}^I = \boldsymbol{V}^P + \boldsymbol{U}(0). \tag{3.9}$$

https://doi.org/10.1017/jfm.2014.559 Published online by Cambridge University Press

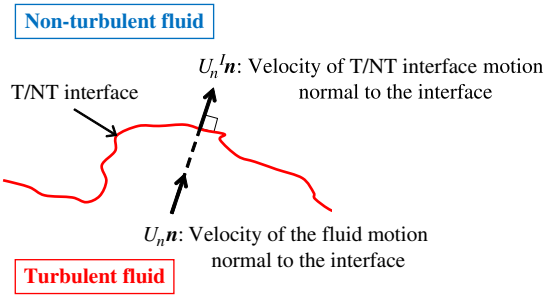


FIGURE 22. (Colour online) Definition of the velocity normal to the T/NT interface.

According to Holzner & Lüthi (2011), $\boldsymbol{V}^P$ is represented by

$$\boldsymbol{V}^P = \left(\frac{2\omega_i \mathcal{S}_{ij} \omega_j}{|\nabla \omega^2|} + \frac{2\nu \omega_i \nabla^2 \omega_i}{|\nabla \omega^2|} \right) \boldsymbol{n}. \tag{3.10}$$

The velocity component of the interface motion normal to the interface, U_n^I, can be obtained as the inner product $U_n^I = \boldsymbol{U}^I \cdot \boldsymbol{n}$. Similarly, the velocity component of fluid normal to the interface, U_n, can be obtained as $U_n(y_I) = \boldsymbol{U}(y_I) \cdot \boldsymbol{n}$.

We investigate the relative velocity between the motions of the interface and of the turbulent fluid, which is defined as $\Delta U_n(y_I) = U_n(y_I) - U_n^I$. The unit normal vector $\boldsymbol{n}$ is defined as positive in the direction of the non-turbulent flow. Turbulent fluid is located in the region $y_I < 0$. Therefore, when $\Delta U_n(y_I) > 0$, the turbulent fluid at y_I approaches the T/NT interface. In contrast, when $\Delta U_n(y_I) < 0$, the T/NT interface moves in the interface normal direction away from the turbulent fluid at y_I. Figure 23(*a*) shows the conditional average of ΔU_n. At the T/NT interface ($y_I = 0$), the relative velocity is equal to the local entrainment velocity, $\Delta U_n = -V^P$, where $V^P \equiv \boldsymbol{V}^P \cdot \boldsymbol{n}$. As shown in figure 23(*a*), $\langle \Delta U_n \rangle_I$ is negative at $y_I = 0$. Thus, the T/NT interface propagates toward the non-turbulent region on average because $\langle V^P \rangle_I$ is positive at the interface. The relative velocity ΔU_n in the turbulent region strongly depends on the interface orientation: near the cross-streamwise and leading edges, $\langle \Delta U_n \rangle_I$ is positive, and the turbulent fluid near these two edges approaches the interface on average; in contrast, $\langle \Delta U_n \rangle_I$ is negative and small in the turbulent region near the trailing edge. Figure 23(*b*) shows the PDF of ΔU_n at $y_I/\lambda = -0.6$. Near the cross-streamwise and leading edges, the PDF preferentially maps positive and large ΔU_n, indicating that the turbulent fluid near these two edges frequently moves rapidly toward the interface. In contrast, turbulent fluid does not often move toward the interface near the trailing edge.

The relative velocity is represented by $\Delta U_n(y_I) = U_n(y_I) - U_n(0) - V^P$. To investigate whether it is determined by the fluid velocity difference $U_n(y_I) - U_n(0)$ or the local entrainment velocity $-V^P$, the PDFs of $U_n(y_I) - U_n(0)$ at $y_I/\lambda = -0.6$ and $-V^P$ are compared in figure 24. The fluid velocity difference is not small at $y_I/\lambda = -0.6$. Additionally, the large relative velocity is caused by the large fluid velocity difference. Thus, the fluid velocity difference makes a much larger contribution to the relative velocity even near the T/NT interface.

The difference in ΔU_n among the three interface orientations can be explained by considering the interface geometry in the jet, which is shown in figure 6. The turbulent fluid in the jet is characterized by larger streamwise velocity than the non-turbulent

https://doi.org/10.1017/jfm.2014.559 Published online by Cambridge University Press

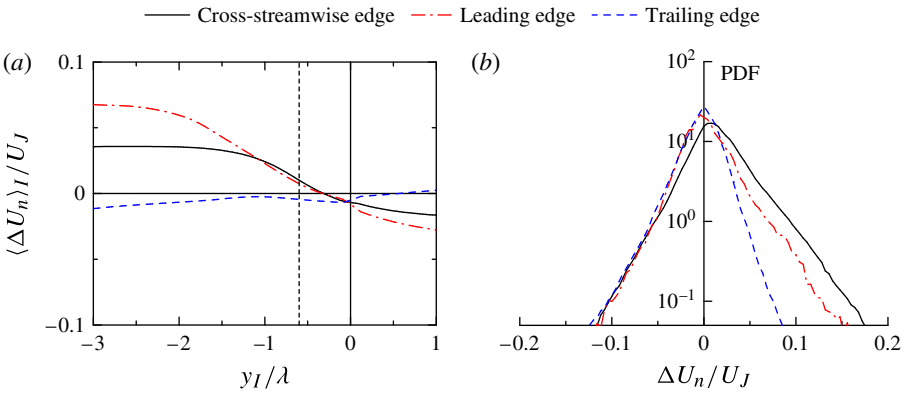


FIGURE 23. (Colour online) (*a*) Conditional average of the relative velocity $\Delta U_n = U_n - U_n^I$ near the cross-streamwise, leading and trailing edges. (*b*) PDF of ΔU_n at $y_I/\lambda = -0.6$ near the cross-streamwise, leading and trailing edges.

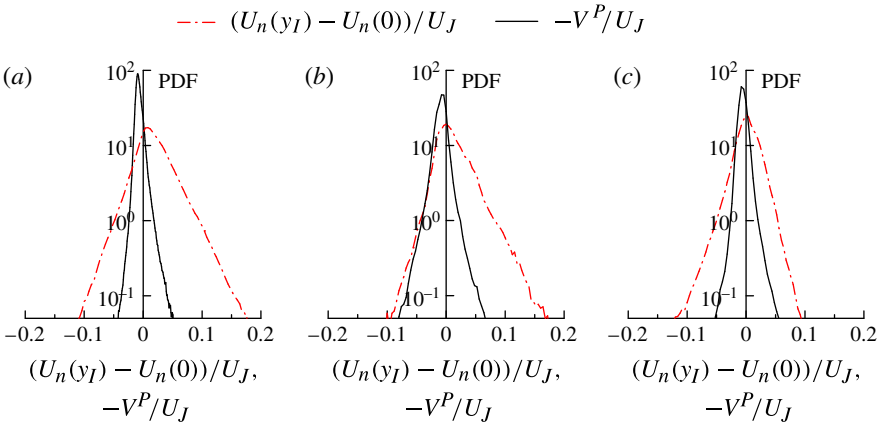


FIGURE 24. (Colour online) Comparison of PDFs of fluid velocity difference and local entrainment velocity near the T/NT interface ($y_I/\lambda = -0.6$): (*a*) cross-streamwise edge; (*b*) leading edge; (*c*) trailing edge.

fluid in the ambient flow. Therefore, the motion of turbulent fluid in the streamwise direction, which is the direction normal to the leading and trailing edges, is faster than the T/NT interface movement in the streamwise direction. Near the leading edge, the turbulent fluid is located upstream of the leading edge, as shown in figure 6, and the velocity difference ΔU_n tends to be positive. In contrast, the turbulent fluid is located downstream of the trailing edge and tend to move away from it, resulting in negative ΔU_n. For the cross-streamwise edge, ΔU_n is calculated from the cross-streamwise (y) component of the velocity. Because the jet expands in the cross-streamwise direction as it develops, the cross-streamwise velocity of the turbulent fluid tends to point in the direction of the ambient flow. The non-turbulent fluid moves toward the jet because of engulfing motion and induced flow in the ambient flow (Philip & Marusic 2012). Because of these opposite motions of turbulent and non-turbulent fluid in the cross-streamwise direction, the turbulent fluid approaches the T/NT interface, and ΔU_n tends to be positive in the turbulent region near the cross-streamwise edge.

https://doi.org/10.1017/jfm.2014.559 Published online by Cambridge University Press

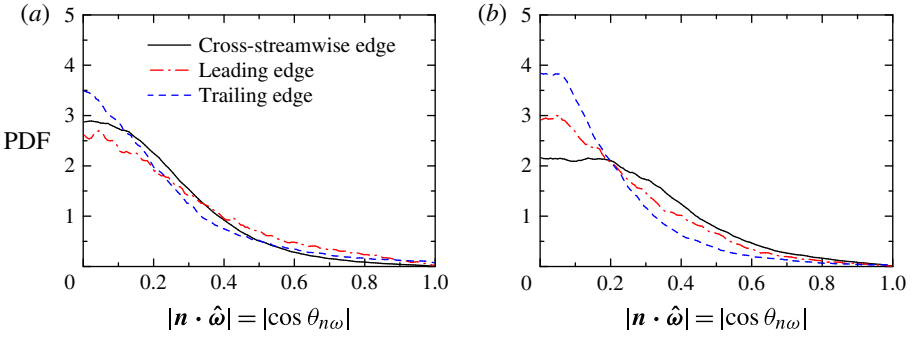


FIGURE 25. (Colour online) Conditional PDF of cosine of alignment angle between the unit normal vector to the T/NT interface ($\boldsymbol{n}$) and the vorticity vector ($\hat{\boldsymbol{\omega}}$) near the T/NT interface ($y_I/\lambda = -0.6$). PDF is calculated conditioned on the sign of the relative velocity $\Delta U_n = U_n - U_n^I$. (*a*) $\Delta U_n > 0$; (*b*) $\Delta U_n < 0$.

Thus, the large-scale motions in the jet and ambient flows, such as engulfing motion and induced flow in the non-turbulent region and large streamwise velocity in the turbulent core region, characterize the velocity field near the T/NT interface.

3.6. *Relationship between enstrophy production and velocity field near the T/NT interface*

We investigate the relationship between the enstrophy production and the velocity field near the T/NT interface by analysing the statistics conditioned on the sign of ΔU_n. Figure 25 shows the PDF of $|\cos\theta_{n\omega}|$ at $y_I/\lambda = -0.6$ calculated conditioned on the sign of ΔU_n. For both positive and negative ΔU_n, the vorticity vector aligns perpendicular to $\boldsymbol{n}$, and the vorticity aligns tangential to the interface.

Figure 26 shows the conditional PDF of $|\cos\theta_{\boldsymbol{n}\boldsymbol{e}_i}|$ conditioned on the sign of ΔU_n at $y_I/\lambda = -0.6$. The unconditional PDF is shown in figure 17. The PDFs of $|\cos\theta_{\boldsymbol{n}\boldsymbol{e}_2}|$ for positive and negative ΔU_n are very similar, and the alignment angle between $\boldsymbol{n}$ and $\boldsymbol{e}_2$ is almost independent of the sign of ΔU_n. In contrast, the alignment angle between $\boldsymbol{n}$ and $\boldsymbol{e}_1$ strongly depends on ΔU_n (figure 26*a*). When ΔU_n is positive, the PDF of $|\cos\theta_{\boldsymbol{n}\boldsymbol{e}_1}|$ is large for perpendicular alignment ($|\cos\theta_{\boldsymbol{n}\boldsymbol{e}_1}| \approx 0$) and small for parallel alignment ($|\cos\theta_{\boldsymbol{n}\boldsymbol{e}_1}| \approx 1$). Thus, when $\Delta U_n > 0$, the extensive strain due to s_1 tends to act in the direction tangential to the T/NT interface (perpendicular to $\boldsymbol{n}$). The opposite tendency can be observed for $\boldsymbol{e}_1$ when $\Delta U_n < 0$. Thus, when $\Delta U_n < 0$, $\boldsymbol{e}_1$ does not show a preference for tangential alignment with the T/NT interface. Figure 26(*c*) shows that the alignment angle between $\boldsymbol{n}$ and $\boldsymbol{e}_3$ also depends on the sign of ΔU_n. When $\Delta U_n > 0$, the PDF of $|\cos\theta_{\boldsymbol{n}\boldsymbol{e}_3}|$ has a large peak for parallel alignment ($|\cos\theta_{\boldsymbol{n}\boldsymbol{e}_3}| \approx 1$), and the compressive strain due to s_3 preferentially acts in the direction normal to the T/NT interface. In contrast, for negative ΔU_n, the PDF for parallel alignment between $\boldsymbol{n}$ and $\boldsymbol{e}_3$ is small, and $\boldsymbol{e}_3$ in the direction normal to the T/NT interface can scarcely be observed. Further, $\boldsymbol{e}_3$ often (seldom) aligns tangentially with the interface when $\Delta U_n < 0$ ($\Delta U_n > 0$).

Figure 27 summarizes the relationship between $\boldsymbol{n}$ and $\boldsymbol{e}_i$ near the interface for positive and negative ΔU. For positive ΔU, $\boldsymbol{e}_1$ and $\boldsymbol{e}_2$ are on the plane parallel to the interface, and $\boldsymbol{e}_3$ points in the direction normal to the interface. For negative ΔU_n, although $\boldsymbol{e}_2$ is on the parallel plane, $\boldsymbol{e}_1$ is not. In addition, $\boldsymbol{e}_1$ is inclined away from $\boldsymbol{n}$,

https://doi.org/10.1017/jfm.2014.559 Published online by Cambridge University Press

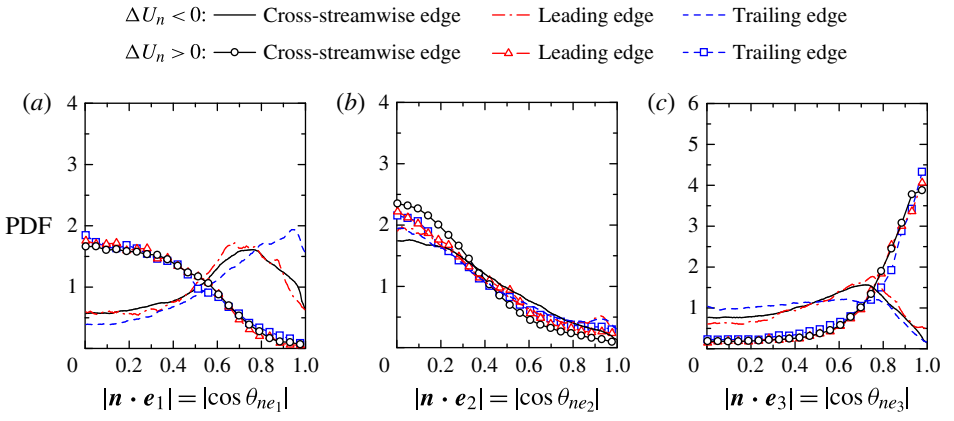


FIGURE 26. (Colour online) Conditional PDF of cosine of alignment angle between the normal vector to the T/NT interface ($\boldsymbol{n}$) and the eigenvectors of the rate-of-strain tensor ($\boldsymbol{e}_i$) near the T/NT interface ($y_I/\lambda = -0.6$). PDF is calculated conditioned on the sign of the relative velocity ΔU_n. (*a*) Extensive strain-rate eigenvector; (*b*) intermediate eigenvector; (*c*) compressive strain-rate eigenvector.

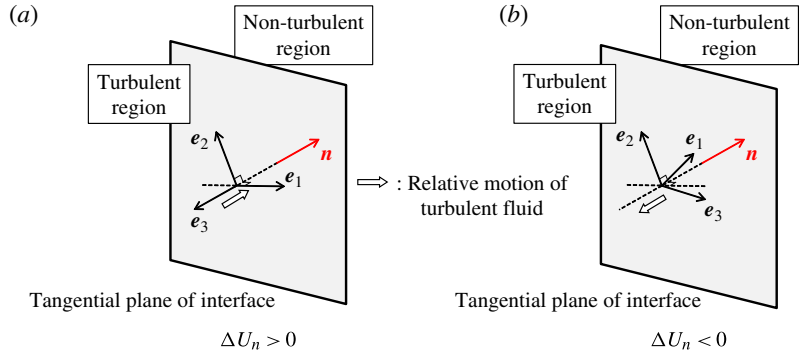


FIGURE 27. (Colour online) Relationship among the interface normal direction, strain-rate eigenvectors and turbulent motion relative to the interface movement for (*a*) positive and (*b*) negative relative velocity ΔU_n.

and $\boldsymbol{e}_3$ does not align with $\boldsymbol{n}$. The vorticity vector is on the plane parallel to the interface for both positive and negative ΔU_n. These tendencies appear for all three interface orientations. The alignment angle between the interface and the strain-rate eigenvectors strongly depends on the sign of ΔU_n but is qualitatively independent of the interface orientation when it is conditioned on the relative velocity. Thus, the alignment between the interface and the strain-rate eigenvectors near the T/NT interface depends on the velocity field near the interface. The unconditional PDFs of $|\cos\theta_{ne_i}|$ (figure 17) for the three interface orientations differ. This difference can be attributed to the dependence of the velocity field ΔU_n on the interface orientation.

The PDF of $|\cos\theta_{\omega e_i}|$ was calculated conditioned on the sign of ΔU_n. Because the alignment between $\boldsymbol{n}$ and $\boldsymbol{e}_2$ is independent of the sign of ΔU_n, the PDF of $|\cos\theta_{\omega e_2}|$ is also independent of ΔU_n. Therefore, we analyse the PDFs of $|\cos\theta_{\omega e_1}|$ (figure 28) and $|\cos\theta_{\omega e_3}|$ (figure 29). The PDF for parallel alignment ($|\cos\theta_{\omega e_1}| \approx 1$) is larger for all three interface orientations when $\Delta U_n > 0$ than when $\Delta U_n < 0$. Perpendicular

https://doi.org/10.1017/jfm.2014.559 Published online by Cambridge University Press

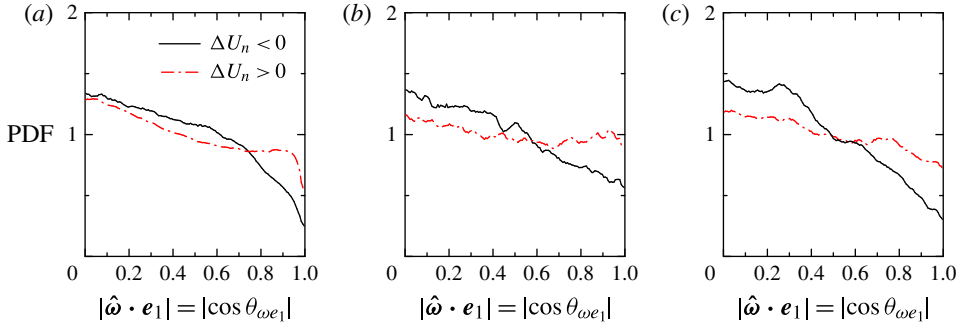


FIGURE 28. (Colour online) Conditional PDF of cosine of alignment angle between the vorticity vector ($\hat{\boldsymbol{\omega}}$) and the extensive strain-rate eigenvector ($\boldsymbol{e}_1$) near the T/NT interface ($y_I/\lambda = -0.6$). PDF is calculated conditioned on the sign of the relative velocity ΔU_n. (*a*) Cross-streamwise edge; (*b*) leading edge; (*c*) trailing edge.

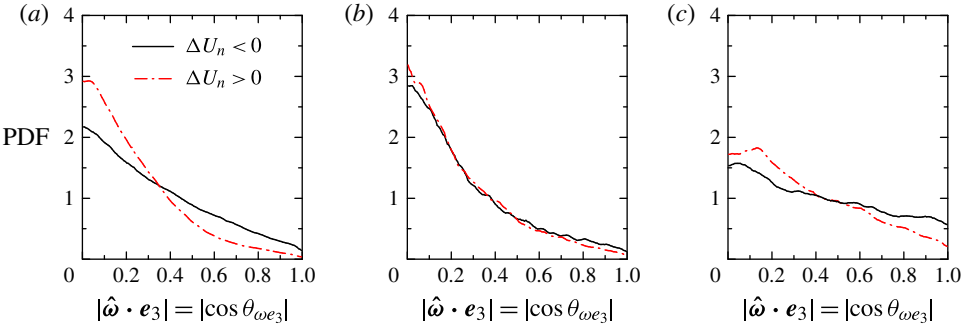


FIGURE 29. (Colour online) Conditional PDF of cosine of alignment angle between the vorticity vector ($\hat{\boldsymbol{\omega}}$) and the compressive strain-rate eigenvector ($\boldsymbol{e}_3$) near the T/NT interface ($y_I/\lambda = -0.6$). PDF is calculated conditioned on the sign of the relative velocity ΔU_n. (*a*) Cross-streamwise edge; (*b*) leading edge; (*c*) trailing edge.

alignment between $\boldsymbol{\omega}$ and $\boldsymbol{e}_3$ appears more frequently when $\Delta U_n > 0$ than when $\Delta U_n < 0$. In contrast, when $\Delta U_n < 0$, $\boldsymbol{e}_3$ often aligns with the vorticity. The dependence of the alignment between $\boldsymbol{\omega}$ and $\boldsymbol{e}_3$ on ΔU_n appears clearly near the cross-streamwise and trailing edges.

The vorticity vector is confined by the T/NT interface and shows a preference for tangential alignment with the interface independently of ΔU_n. When $\Delta U_n > 0$, $\boldsymbol{e}_1$ also tends to be tangential to the interface. Therefore, parallel alignment between $\boldsymbol{e}_1$ and the vorticity vector appears frequently when $\Delta U_n > 0$. Furthermore, when $\Delta U_n > 0$, $\boldsymbol{e}_3$ is often oriented perpendicular to the T/NT interface, resulting in perpendicular alignment between $\boldsymbol{e}_3$ and $\hat{\boldsymbol{\omega}}$. Therefore, when $\Delta U_n > 0$, the extensive strain due to s_1 acts effectively on the vorticity because of the parallel alignment between $\hat{\boldsymbol{\omega}}$ and $\boldsymbol{e}_1$, whereas the compressive strain due to s_3 does not act well because of its perpendicular alignment with the vorticity. In contrast, when $\Delta U_n < 0$, $\boldsymbol{e}_1$ shows no preference for parallel alignment with the vorticity vector, but $\boldsymbol{e}_3$ often acts in the direction parallel to the vorticity vector. This dependence of the alignment between $\hat{\boldsymbol{\omega}}$ and $\boldsymbol{e}_i$ on the sign of ΔU_n can be observed for all three interface orientations. These results show that the alignment angle between the strain-rate eigenvector and the vorticity depends on the velocity field near the T/NT interface.

https://doi.org/10.1017/jfm.2014.559 Published online by Cambridge University Press

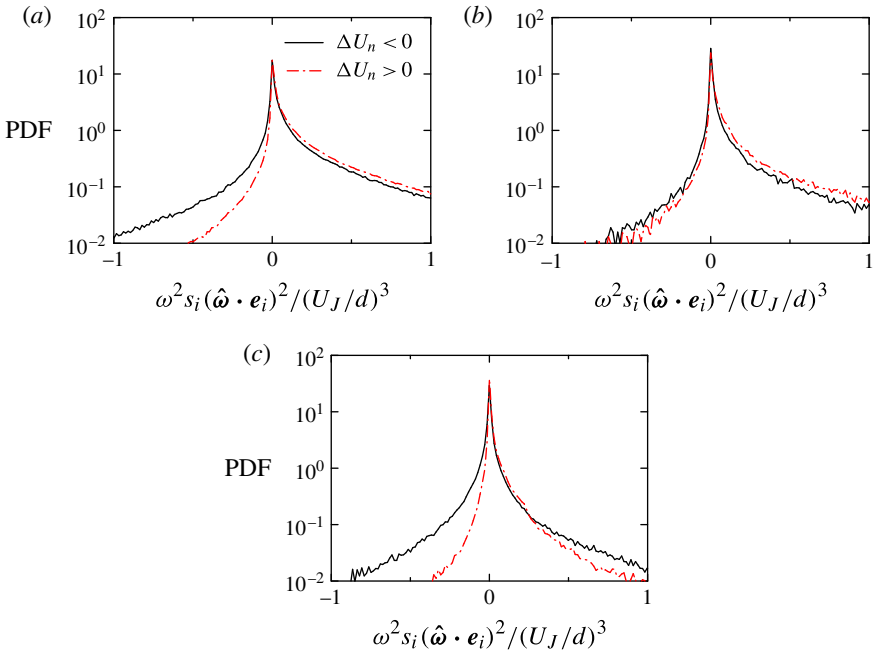


FIGURE 30. (Colour online) Conditional PDF of the enstrophy production term near the T/NT interface ($y_I/\lambda = -0.6$). PDF is calculated conditioned on the sign of the relative velocity $\Delta U_n = U_n - U_n^I$. (*a*) Cross-streamwise edge; (*b*) leading edge; (*c*) trailing edge.

Figure 30 shows the PDF of the enstrophy production $\omega^2 s_i(\hat{\boldsymbol{\omega}} \cdot \boldsymbol{e}_i)^2$ conditioned on the sign of ΔU_n near the T/NT interface ($y_I/\lambda = -0.6$). The PDF for negative $\omega^2 s_i(\hat{\boldsymbol{\omega}} \cdot \boldsymbol{e}_i)^2$ is large when $\Delta U_n < 0$. The difference between positive and negative ΔU_n is small for the leading edge because the alignment angle between $\boldsymbol{e}_3$ and $\hat{\boldsymbol{\omega}}$ differs only slightly between positive and negative ΔU_n (figure 29*b*). Thus, the enstrophy is reduced (negative $\omega^2 s_i(\hat{\boldsymbol{\omega}} \cdot \boldsymbol{e}_i)^2$) mainly when $\Delta U_n < 0$ for all three interface orientations. Further, enstrophy generation (positive $\omega^2 s_i(\hat{\boldsymbol{\omega}} \cdot \boldsymbol{e}_i)^2$) is frequently observed when $\Delta U_n > 0$ near the cross-streamwise and leading edges. These differences between positive and negative ΔU_n can be related to the alignment between the vorticity and the strain-rate eigenvectors. The large enstrophy reduction for negative ΔU_n is caused by the inconsistency between the directions of $\hat{\boldsymbol{\omega}}$ and $\boldsymbol{e}_1$ and the parallel alignment between $\hat{\boldsymbol{\omega}}$ and $\boldsymbol{e}_3$. These alignments between the vorticity and the extensive and compressive strain-rate eigenvectors cause the small enstrophy generation by s_1 and the large enstrophy reduction by s_3 for negative ΔU_n. In contrast, when $\Delta U_n > 0$, vortex stretching by s_1 and compression by s_3 preferentially act in directions parallel and perpendicular to the vorticity, respectively. Thus, enstrophy is produced by vortex stretching by s_1 without being greatly affected by vortex compression.

The vorticity and strain-rate eigenvectors are confined by the T/NT interface. The confinement of the strain field and vorticity causes the difference in the enstrophy production among the interface orientations. The alignment between the strain-rate eigenvectors and the interface orientation depends on the velocity field near the T/NT interface, which is determined mainly by the interface orientation, i.e. the geometry of the T/NT interface. The dependence of the velocity field on the interface orientation

https://doi.org/10.1017/jfm.2014.559 Published online by Cambridge University Press

can be related to the effects of the mean flow and mean shear. The T/NT interface is strongly convoluted, and the convolution is formed by the large-scale motions of the jet and ambient flows. The present results reveal that the enstrophy production near the T/NT interface in the jet is affected by the velocity field near the interface, which strongly depends on the interface geometry, because the relationship between the vorticity and strain field depends on the velocity field near the interface.

4. Conclusion

Vortex stretching and compression, which cause enstrophy production by inviscid processes, have been investigated in the turbulent region near the T/NT interface by using the DNS results for a planar jet. The interface characteristics were analysed individually for three different interface orientations, which are called the cross-streamwise edge, leading edge and trailing edge.

The enstrophy and its production rate strongly depend on the interface orientation near the T/NT interface. Near the cross-streamwise and leading edges, the enstrophy generation by vortex stretching is predominant over the enstrophy reduction by vortex compression. However, both vortex stretching and compression are important near the trailing edge, resulting in the small averaged enstrophy production rate. Analysis of the invariants of velocity gradient tensor and rate-of-strain tensor shows that the strain field near the T/NT interface is significantly different between the trailing edge and the cross-streamwise and leading edges. The visualization of instantaneous flow field shows that the vortex stretching and compression regions near the T/NT interface appear as sheet-like structures and small spots, respectively.

The enstrophy production was investigated by analysing the relationship among a vorticity vector, strain-rate eigenvectors and eigenvalues. The orientation of vorticity near the T/NT interface is confined in the tangential direction to the interface. The strain-rate eigenvectors are also confined by the interface. Near the cross-streamwise and leading edges, vortex compression by the compressive strain-rate eigenvalue s_3 acts ineffectively on the vorticity because of the perpendicular alignment between the eigenvector for s_3 and the vorticity. In contrast, vortex compression by s_3 acts effectively on the vorticity near the trailing edge because of the parallel alignment between the eigenvector for s_3 and the vorticity. The enstrophy production near the trailing edge is small because of the weak intensity of vortex stretching and the vortex compression acting effectively. Thus, vortex stretching and compression significantly depend on the characteristics of the T/NT interface, around which the vorticity vector and strain-rate eigenvectors are confined by the presence of the T/NT interface.

The statistics were calculated conditioned on the motion of turbulent fluid relative to that of the T/NT interface. The alignment between the interface and the strain-rate eigenvectors near the T/NT interface changes depending on the velocity field near the interface. When the turbulent fluid relatively moves toward the T/NT interface, the vorticity shows a preference for parallel and perpendicular alignments with the extensive and compressive strain-rate eigenvectors, respectively. In this case, the enstrophy is generated by vortex stretching without being greatly affected by vortex compression by s_3. For the turbulent fluid moving away from the interface, the opposite alignment can be observed between the vorticity and the extensive and compressive strain-rate eigenvectors. Therefore, vortex compression acts effectively on the vorticity, whereas vortex stretching does not act well. Because of these alignments, large enstrophy reduction arises when the turbulent fluid moves away from the interface. This alignment tendency can be observed for the three interface

https://doi.org/10.1017/jfm.2014.559 Published online by Cambridge University Press

orientations. The geometrical effects on the velocity field near the interface can be related to the effects of the mean flow and mean shear. Thus, the enstrophy production near the T/NT interface strongly depends on the velocity field near the interface because the alignment between the vorticity and the strain-rate eigenvectors changes depending on the velocity field near the interface.

Acknowledgements

The authors acknowledge Professor C. B. da Silva and Mr R. R. Taveira for providing valuable comments. The authors also acknowledge the anonymous referees for valuable comments. The authors would like to thank Dr O. Terashima for his help in this study. Part of this work was conducted under the Collaborative Research Project of the Institute of Fluid Science, Tohoku University. This work was supported by JSPS KAKENHI grant number 25002531 and MEXT KAKENHI grant numbers 25289030, 25289031 and 25630052.

REFERENCES

ASHURST, W. T., KERSTEIN, A. R., KERR, R. M. & GIBSON, C. H. 1987 Alignment of vorticity and scalar gradient with strain rate in simulated Navier–Stokes turbulence. *Phys. Fluids* **30** (8), 2343–2353.

BISSET, D. K., HUNT, J. C. R. & ROGERS, M. M. 2002 The turbulent/non-turbulent interface bounding a far wake. *J. Fluid Mech.* **451**, 383–410.

BLACKBURN, H. M., MANSOUR, N. N. & CANTWELL, B. J. 1996 Topology of fine-scale motions in turbulent channel flow. *J. Fluid Mech.* **310**, 269–292.

BRADBURY, L. J. S. 1965 The structure of a self-preserving turbulent plane jet. *J. Fluid Mech.* **23**, 31–64.

BUXTON, O. R. H. & GANAPATHISUBRAMANI, B. 2010 Amplification of enstrophy in the far field of an axisymmetric turbulent jet. *J. Fluid Mech.* **651**, 483–502.

CHAUHAN, K., PHILIP, J., DE SILVA, C. M., HUTCHINS, N. & MARUSIC, I. 2014 The turbulent/non-turbulent interface and entrainment in a boundary layer. *J. Fluid Mech.* **742**, 119–151.

CORRSIN, S. & KISTLER, A. L. 1955 Free-stream boundaries of turbulent flows. *NACA Tech. Rep.* TN-1244.

DAI, Y., KOBAYASHI, T. & TANIGUCHI, N. 1994 Large eddy simulation of plane turbulent jet flow using a new outflow velocity boundary condition. *JSME Intl J.* B **37** (2), 242–253.

DAVIDSON, P. A. 2004 *Turbulence: An Introduction for Scientists and Engineers*. Oxford University Press.

DAVIES, A. E., KEFFER, J. F. & BAINES, W. D. 1975 Spread of a heated plane turbulent jet. *Phys. Fluids* **18** (7), 770–775.

DEO, R. C., MI, J. & NATHAN, G. J. 2008 The influence of Reynolds number on a plane jet. *Phys. Fluids* **20** (7), 075108.

GUTMARK, E. & WYGNANSKI, I. 1976 The planar turbulent jet. *J. Fluid Mech.* **73** (3), 465–495.

HOLZNER, M., LIBERZON, A., NIKITIN, N., LÜTHI, B., KINZELBACH, W. & TSINOBER, A. 2008 A Lagrangian investigation of the small-scale features of turbulent entrainment through particle tracking and direct numerical simulation. *J. Fluid Mech.* **598**, 465–475.

HOLZNER, M. & LÜTHI, B. 2011 Laminar superlayer at the turbulence boundary. *Phys. Rev. Lett.* **106** (13), 134503.

JIMÉNEZ, J. 1992 Kinematic alignment effects in turbulent flows. *Phys. Fluids* A **4** (4), 652–654.

KEMPF, A., KLEIN, M. & JANICKA, J. 2005 Efficient generation of initial- and inflow-conditions for transient turbulent flows in arbitrary geometries. *Flow Turbul. Combust.* **74** (1), 67–84.

KLEIN, M., SADIKI, A. & JANICKA, J. 2003 Investigation of the influence of the Reynolds number on a plane jet using direct numerical simulation. *Intl J. Heat Fluid Flow* **24** (6), 785–794.

https://doi.org/10.1017/jfm.2014.559 Published online by Cambridge University Press

MORINISHI, Y., LUND, T. S., VASILYEV, O. V. & MOIN, P. 1998 Fully conservative higher order finite difference schemes for incompressible flow. *J. Comput. Phys.* **143** (1), 90–124.

MUNGAL, M. G. & HOLLINGSWORTH, D. K. 1989 Organized motion in a very high Reynolds number jet. *Phys. Fluids* A **1** (10), 1615–1623.

OOI, A., MARTIN, J., SORIA, J. & CHONG, M. S. 1999 A study of the evolution and characteristics of the invariants of the velocity-gradient tensor in isotropic turbulence. *J. Fluid Mech.* **381**, 141–174.

PHILIP, J. & MARUSIC, I. 2012 Large-scale eddies and their role in entrainment in turbulent jets and wakes. *Phys. Fluids* **24** (5), 055108.

PHILIP, J., MENEVEAU, C., DE SILVA, C. M. & MARUSIC, I. 2014 Multiscale analysis of fluxes at the turbulent/non-turbulent interface in high Reynolds number boundary layers. *Phys. Fluids* **26** (1), 015105.

RAMAPRIAN, B. R. & CHANDRASEKHARA, M. S. 1985 LDA measurements in plane turbulent jets. *Trans. ASME: J. Fluids Engng* **107** (2), 264–271.

VAN REEUWIJK, M. & HOLZNER, M. 2014 The turbulence boundary of a temporal jet. *J. Fluid Mech.* **739**, 254–275.

DA SILVA, C. B. & DOS REIS, R. J. N. 2011 The role of coherent vortices near the turbulent/non-turbulent interface in a planar jet. *Phil. Trans. R. Soc. Lond.* A **369**, 738–753.

DA SILVA, C. B., DOS REIS, R. J. N. & PEREIRA, J. C. F. 2011 The intense vorticity structures near the turbulent/non-turbulent interface in a jet. *J. Fluid Mech.* **685**, 165–190.

DA SILVA, C. B., HUNT, J. C. R., EAMES, I. & WESTERWEEL, J. 2014 Interfacial layers between regions of different turbulence intensity. *Annu. Rev. Fluid Mech.* **46**, 567–590.

DA SILVA, C. B. & PEREIRA, J. C. F. 2004 The effect of subgrid-scale models on the vortices computed from large-eddy simulations. *Phys. Fluids* **16** (12), 4506–4534.

DA SILVA, C. B. & PEREIRA, J. C. F. 2008 Invariants of the velocity-gradient, rate-of-strain, and rate-of-rotation tensors across the turbulent/nonturbulent interface in jets. *Phys. Fluids* **20** (5), 055101.

DA SILVA, C. B. & TAVEIRA, R. R. 2010 The thickness of the turbulent/nonturbulent interface is equal to the radius of the large vorticity structures near the edge of the shear layer. *Phys. Fluids* **22** (12), 121702.

DE SILVA, C. M., PHILIP, J., CHAUHAN, K., MENEVEAU, C. & MARUSIC, I. 2013 Multiscale geometry and scaling of the turbulent-nonturbulent interface in high Reynolds number boundary layers. *Phys. Rev. Lett.* **111** (4), 044501.

SORIA, J., SONDERGAARD, R., CANTWELL, B. J., CHONG, M. S. & PERRY, A. E. 1994 A study of the fine-scale motions of incompressible time-developing mixing layers. *Phys. Fluids* **6** (2), 871–884.

SPALART, P. R., MOSER, R. D. & ROGERS, M. M. 1991 Spectral methods for the Navier–Stokes equations with one infinite and two periodic directions. *J. Comput. Phys.* **96** (2), 297–324.

STANLEY, S. A., SARKAR, S. & MELLADO, J. P. 2002 A study of the flow-field evolution and mixing in a planar turbulent jet using direct numerical simulation. *J. Fluid Mech.* **450**, 377–407.

TANAHASHI, M., IWASE, S. & MIYAUCHI, T. 2001 Appearance and alignment with strain rate of coherent fine scale eddies in turbulent mixing layer. *J. Turbul.* **2** (6), 1–18.

TAVEIRA, R. R., DIOGO, J. S., LOPES, D. C. & DA SILVA, C. B. 2013 Lagrangian statistics across the turbulent–nonturbulent interface in a turbulent plane jet. *Phys. Rev.* E **88** (4), 043001.

TAVEIRA, R. R. & DA SILVA, C. B. 2014 Characteristics of the viscous superlayer in shear free turbulence and in planar turbulent jets. *Phys. Fluids* **26** (2), 021702.

TOWNSEND, A. A. 1976 *The Structure of Turbulent Shear Flow*. Cambridge University Press.

WATANABE, T., SAKAI, Y., NAGATA, K., ITO, Y. & HAYASE, T. 2014*a* Wavelet analysis of coherent vorticity near the turbulent/non-turbulent interface in a turbulent planar jet. *Phys. Fluids* **26** (9), 095105.

WATANABE, T., SAKAI, Y., NAGATA, K. & TERASHIMA, O. 2013*a* Joint statistics between velocity and reactive scalar in a turbulent liquid jet with a chemical reaction. *Phys. Scr.* **T155**, 014039.

WATANABE, T., SAKAI, Y., NAGATA, K. & TERASHIMA, O. 2014*b* Experimental study on the reaction rate of a second-order chemical reaction in a planar liquid jet. *AIChE J.* **60** (11), 3969–3988.

https://doi.org/10.1017/jfm.2014.559 Published online by Cambridge University Press

WATANABE, T., SAKAI, Y., NAGATA, K. & TERASHIMA, O. 2014*c* Turbulent Schmidt number and eddy diffusivity change with a chemical reaction. *J. Fluid Mech.* **754**, 98–121.

WATANABE, T., SAKAI, Y., NAGATA, K., TERASHIMA, O. & KUBO, T. 2012 Simultaneous measurements of reactive scalar and velocity in a planar liquid jet with a second-order chemical reaction. *Exp. Fluids* **53** (5), 1369–1383.

WATANABE, T., SAKAI, Y., NAGATA, K., TERASHIMA, O., SUZUKI, H., HAYASE, T. & ITO, Y. 2013*b* Visualization of turbulent reactive jet by using direct numerical simulation. *Intl J. Model. Simul. Sci. Comput.* **4**, 1341001.

WESTERWEEL, J., FUKUSHIMA, C., PEDERSEN, J. M. & HUNT, J. C. R. 2005 Mechanics of the turbulent-nonturbulent interface of a jet. *Phys. Rev. Lett.* **95** (17), 174501.

WESTERWEEL, J., FUKUSHIMA, C., PEDERSEN, J. M. & HUNT, J. C. R. 2009 Momentum and scalar transport at the turbulent/non-turbulent interface of a jet. *J. Fluid Mech.* **631**, 199–230.

WESTERWEEL, J., HOFMANN, T., FUKUSHIMA, C. & HUNT, J. C. R. 2002 The turbulent/non-turbulent interface at the outer boundary of a self-similar turbulent jet. *Exp. Fluids* **33** (6), 873–878.

WOLF, M., LÜTHI, B., HOLZNER, M., KRUG, D., KINZELBACH, W. & TSINOBER, A. 2012 Investigations on the local entrainment velocity in a turbulent jet. *Phys. Fluids* **24** (10), 105110.

ZHOU, Y., NAGATA, K., SAKAI, Y., SUZUKI, H., ITO, Y., TERASHIMA, O. & HAYASE, T. 2014 Development of turbulence behind the single square grid. *Phys. Fluids* **26** (4), 045102.

https://doi.org/10.1017/jfm.2014.559 Published online by Cambridge University Press